



UNIVERSITEIT VAN AMSTERDAM



VRIJE
UNIVERSITEIT
AMSTERDAM

Bachelor Thesis Natuur- en Sterrenkunde

Strain engineering of 2D KIB anode materials

by

Tera Molenaar

July 4th 2025

Abstract

Material design has been widely utilized to tune physical and chemical properties of materials, broadening their use in application. In the semiconductor industry, strain engineering has widely been used to tune physical properties by deformation of materials through inducing strain.[1] Moreover, this method has been shown to be applicable for the enhancement of rechargeable batteries, namely sodium and lithium ion batteries.[2] This work focuses on elucidating the effect of strain on potassium ion battery (KIB) performance, through strain engineering a diverse set of 2D KIB anode materials, allowing for a systematic comparative study on the applicability of strain engineering in enhancing KIB performance. A computational study based on density functional theory (DFT) was performed to simulate biaxial strains onto the materials, evaluating the effect on properties relating to anode performance. The properties that were assessed included the propensity to form vacancy defects, potassium adsorption energetics, and electronic structure (as a proxy for electrical conductivity). In this work, it was found that strain engineering shows to be an applicable method in enhancing the prospects of 2D anode materials. In particular, this was shown for the effect of strain relating to potassium adsorption, showing a significant strengthening of adsorption energy for the +10% strained models, namely 36% for graphene, 32% for silicene, and 12% for phosphorene. Moreover, it was found that the introduction of vacancy defects could additionally contribute to increasing potassium storage. In the application of strain engineering as a method, applying tensile strains showed to be the most favorable, as the results for the compressive strained models showed a propensity for significant structural changes and disorder.

Student number

14658046

Research institute

ARCNL & ITFA

Research group

Materials Theory and Modelling

Examiner

Paul Planken

Supervisor

Emilia Olsson

Contents

Populaire wetenschappelijke samenvatting	3
1 Introduction	4
2 Methodology	6
2.1 Convergence tests	6
2.2 Choice of exchange-correlation functional	7
2.3 Setup of strained models	8
2.4 Vacancy formation energy	9
2.5 Adsorption energy	9
2.6 Bader charges	9
2.7 Electronic properties	10
3 Results	10
3.1 Pristine models	10
3.2 Strain engineering of undefective models	11
3.2.1 Structural changes as a function of strain	12
3.2.2 Electronic structure changes as a function of strain	13
3.3 Vacancy strain engineering	14
3.4 Potassium Adsorption	17
3.4.1 Defective models	18
3.4.2 Strain engineering	19
3.4.3 Electronic structure	21
4 Conclusion	21
5 Future research	22
Acknowledgements	22
References	23
Appendix A: Convergence Tests	28
Appendix B: Structural Parameters	31
Appendix C: Strain engineering	32
Appendix D: Vacancy formation energy	33
Appendix E: Adsorption energy	34
Appendix F: Electronic structures	35
Appendix G: Bader charges	39

Populaire wetenschappelijke samenvatting

Oplaadbare batterijen spelen een belangrijke rol in het dagelijks leven. Ze worden gebruikt in mobiele telefoons, laptops, elektrische voertuigen en medische toepassingen.[3][4] Bovendien zijn oplaadbare batterijen belangrijk in het efficiënt kunnen gebruiken van wind en zonne-energie om de CO₂-uitstoot wereldwijd te verminderen.[5] De meeste oplaadbare batterijen die worden gebruikt zijn lithium-ion batterijen.[6] Het aanbod van lithium is echter gelimiteerd terwijl de vraag naar batterijen toeneemt.[7][8] Omdat kalium veel voorkomt, focust dit werk zich op de toepassing van kalium-ion batterijen.[6][9]

In figuur 1 wordt de kalium-ion batterij (KIB) weergegeven waarbij de drie belangrijkste componenten staan aangegeven: de anode, de kathode en de elektrolyt. Als de batterij wordt gebruikt, bewegen de kalium ionen (paarse cirkels) van de anode naar de kathode.[6] De elektronen worden buiten de batterij getransporteerd, wat zorgt voor het opwekken van elektrische energie (zie e⁻ in figuur 1).[6] Veel onderzoek wordt gedaan naar deze componenten om de prestatie van batterijen te verbeteren.

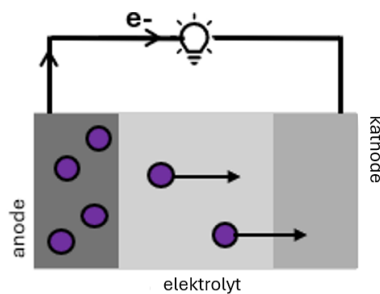


Figure 1: De kalium-ion batterij weergegeven met de drie belangrijkste componenten: de anode, de kathode, en de elektrolyt. De kalium atomen zijn weergegeven met paarse cirkels en de elektronen met e⁻.

Dit onderzoek focust zich op de methode van ‘strain engineering’ om eigenschappen van de anode aan te passen en daarmee mogelijk te verbeteren. Strain engineering is een methode waarbij een materiaal wordt vervormd door het uit te rekken of in te drukken, waardoor eigenschappen van het materiaal veranderen. Er is gekozen om het effect van ‘strain engineering’ te onderzoeken op twee dimensionale (2D) materialen. Dit is omdat 2D materialen makkelijk kunnen worden uitgerekt en ingedrukt.[1] Bovendien zijn ze veelbelovend voor de toepassing als anode in kalium-ion batterijen.[10]

Het effect van ‘strain engineering’ is bepaald door te kijken naar de eigenschappen van de geselecteerde materialen die belangrijk zijn voor de toepassing van kalium-ion batterijen. Deze eigenschappen zijn gerelateerd aan de stabiliteit van het materiaal, de capaciteit voor de opslag van kalium ionen, en hoe goed het materiaal stroom kan geleiden. Dit is ten eerste onderzocht voor modellen van de reguliere 2D materialen. Vervolgens zijn deze modellen aangepast om de materialen te beschrijven als ze worden uitgerekt of ingedrukt om het effect van ‘strain engineering’ te begrijpen. De vergelijking van de aangepaste modellen met de reguliere modellen laat zien of de verbetering van KIB anode materialen mogelijk is door middel van ‘strain engineering’.

Als resultaat laat dit onderzoek zien dat ‘strain engineering’ een toepasbare methode is om de prestatie van kalium-ion batterijen te verbeteren. Het uitrekken van de materialen resulteerde namelijk in een toename van de affiniteit voor het adsorberen van kalium ionen met een hoogste toename van 36%. Dit wijst erop dat de capaciteit voor de opslag van kalium ionen kan toenemen door het uitrekken van een anode materiaal, wat de prestatie van een kalium-ion batterij verbetert. De methode van ‘strain engineering’ biedt daarom uitkomst voor het verbeteren van de toepassing van kalium-ion batterijen als alternatief voor lithium-ion batterijen.

1 Introduction

Rechargeable batteries are widely used in various applications such as mobile phones, electrical vehicles and medical implants.[3][4] Energy storage technologies, including rechargeable batteries, are of great importance in the employment of renewable energy sources, and the reduction of worldwide carbon emission.[5] Currently, the lithium ion battery is the most common rechargeable battery, due to its high energy density.[6] However, in contrast to the increasing demand of batteries, the supply of lithium is limited, which may become an issue in the future.[7][8] An alternative could be provided by the use of potassium in so called potassium ion batteries (KIBs), provided with the advantage of potassium being an abundant resource.[6][9]

Batteries contain three main components, the cathode, the anode and the electrolyte, as illustrated in figure 2. The electrolyte serves as a barrier between the two electrodes, allowing for the movement of potassium ions, while hindering the movement of electrons. Typically for KIBs, potassium is provided by the cathode.[6] As illustrated in figure 2, charging the battery involves the transport of potassium ions through the electrolyte to the anode. When the battery is discharged, the potassium ions move back to the cathode, while the electrons are transported along an external circuit, generating a current.[6]

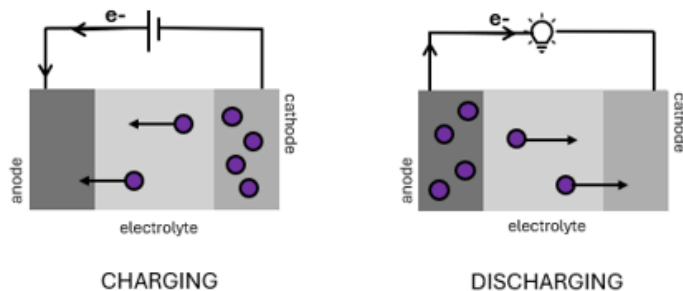


Figure 2: A schematic overview of electron and potassium (purple spheres) displacement in KIBs upon charging and discharging.

The anode plays a crucial role in the electrochemical performance of batteries.[6] With respect to that, properties of the anode such as electrical conductivity, structural stability and specific capacity are considered to be of importance, where specific capacity refers to how much charge per unit can be stored.[11][6] For the application of commercially produced LIBs, graphite materials are utilized.[12] However, graphite materials are known to have a relatively low theoretical capacity, with a value of 372 mAh/g for lithium storage capacity.[12][13] Initially carbonaceous materials were investigated for the application of KIBs as well, where likewise the limited capacity comprises a disadvantage, with a value of 279 mAh/g.[6][14] Hence, the development of anodes that have higher potassium storage capacity is considered of importance.[6] In the light of higher potassium storage capacity, both phosphorus-based materials and silicon have been considered promising candidates for KIB application.[6][15] Silicon shows a high capacity of 995 mAh/g in the form of KSi, and phosphorus has a significantly high theoretical capacity of 2,596 mAh/g for lithium and sodium ion batteries.[15][16] However, for the application of both materials as KIB anode, challenges arise as phosphorus is structurally instable at ambient conditions and silicon is prone to anode degradation upon insertion and extraction of atoms.[17][15] Additionally, focus lies on improving the low conductivity and structural stability of KIB anodes that arises due to the extraction and insertion of relatively large K-ions upon battery applications.[6]

In respect to these challenges, 2D materials show a lot of promise for the application of KIB anodes, as they contain a larger specific surface area than their 3D counterparts.[10] This allows for an increased number of active sites for K^+ ion storage, and adaption to volume variation caused by the insertion and extraction of potassium atoms.[10][6]

In this work, three 2D materials were selected based on their prospects in the application of KIB batteries, as shown in figure 3. The first material we focus on is graphene, as its bulk graphite form is widely used as an anode in LIBs, and has shown a lot of promise also for KIBs.[18][10] Graphene is a widely studied nanomaterial with a planar hexagonal structure made out of carbon atoms.[19][10] It is a strong material with remarkable mechanical properties and high electrical conductivity.[20][19] However, the relatively low theoretical maximum for its storage capacity of potassium (278 mAh/g) is a disadvantage in its use for KIB applications.[21][10]

A high capacity is of importance for the electrochemical performance of KIBs. Therefore, materials with a higher (theoretical) capacity were additionally selected, namely silicene (716 mAh/g) and phosphorene (2,695 mAh/g).[22][16][23] Silicene, has a buckled hexagonal structure, and calculations have shown that it could be a suitable anode for various metal ion batteries, among which are the KIBs.[24][10][25] However, the application of silicene as an anode comes with obstacles, such as the susceptibility to fracture as a result of mechanical stress.[22] For the third anode material investigated in this thesis, phosphorene was selected, which is a monolayer of phosphorus with a highly buckled structure.[26] As mentioned, phosphorus has a significantly higher theoretical capacity of 2,596 mAh/g for lithium and sodium ion batteries.[16] In comparison to red phosphorus, phosphorene has been shown to contain a higher capacity for lithium and sodium ion batteries.[23] However, as for silicene, the application of phosphorene comes with obstacles due to its instability.[23]

To improve the electrochemical performance of anodes in KIBS, various efforts have been made using strategies such as structural design and morphology control.[10] Another method that has been used to tune physical properties is strain engineering.[1] Strain is considered a measure of deformation, as it is defined by the fractional change in length.[27] Therefore, strain engineering consists of inducing strain into a material, resulting in deformation. Strain engineering has already been widely utilized in the semiconductor industry.[1] For energy storage applications, strain engineering could likewise be a successful method as illustrated by the research of Hao et al.[2] This study showed that tensile strain can be applied to increase Li and Na adsorption on monolayer MoS₂, and that a similar method could be applied, to enhance battery performance, to other stretchable low-dimensional nanomaterials.[2] The computational study of Hao et al. illustrated the applicability of strain engineering low-dimensional nanomaterials to enhance battery performance for LIBs and SIBs.[2] Hence, this work aims to elucidate the expected effect of this method, with a specific focus on the enhancement of KIB performance.

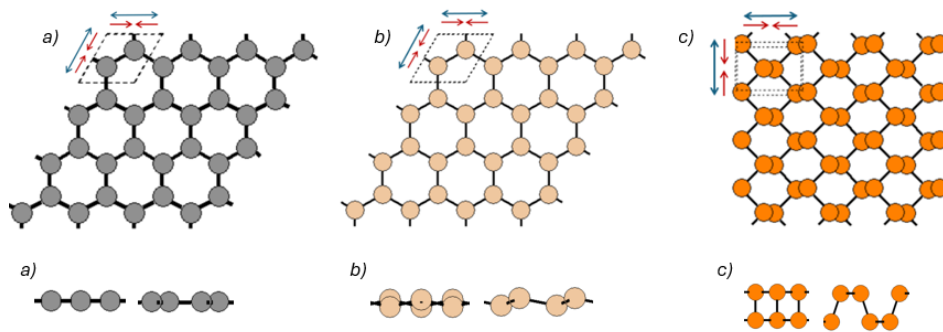


Figure 3: The front and side views of the studied materials, a) graphene, b) silicene, and c) phosphorene, are shown with the applied strain. The grey circles therefore represent carbon atoms, the beige circles silicon atoms, and the orange circles phosphorus atoms. The blue arrows illustrates the applied tensile strain, while the red arrows represent the compressive strain.

By performing a computational study, the effect of strain can be systematically assessed for a wide range of properties and 2D anode materials, with the most promising ones then fed into experimental and device optimisation. The strain engineering of 2D materials shows specifically a lot

of promise, due to a stronger deformation capacity, a larger variety of deformation methods, and a higher sensitivity to strain, in comparison to bulk materials.[1] Silicene, graphene, and phosphorene include a diverse set of 2D KIB anodes with varying characteristics, including degree of puckering and electrical conductivity, making them an ideal set for a systematic comparative study on the applicability of strain engineering for 2D anodes. This contributes in evaluating whether the method of strain engineering gives rise to a general effect on 2D KIB anodes in the light of enhancing battery performance. Additionally, individual differences between the effect of strain on the anodes can be possibly related to their varied characteristics.

In light of enhancing battery performance, the properties of the materials that will be studied relate to their application in KIBs. These properties include electronic properties, the formation of vacancy defects, and potassium adsorption. The study on the formation of structural defects is limited to the study of vacancy defects, as they are among the most common in 2D materials.[28] By means of an atomic scale computational study, this work aims to contribute to the motivation for performing experimental studies on strain engineered 2D materials, with the expectation of improving the application prospects of KIB anodes.

In this work, we will assess the selected materials based on electronic structure (as a proxy of electrical conductivity), their propensity to form vacancy defects, and potassium adsorption energetics. Subsequently, biaxial compressive and tensile strains will be applied to the various pristine models, as shown in figure 3, to elucidate the effect of strain engineering on the highlighted metrics. The results for each of the properties will show whether the applied strain results in a general effect across the different anode materials or whether individual differences, such as in composition or structure, play a more significant role.

2 Methodology

In this thesis, all simulations are performed using density functional theory (DFT), which introduces the concept of electron density as an approach to solving the Schrödinger equation for many-atom and many-electron systems, such as 2D materials.[29] DFT has been important in understanding phenomena underlying physical properties and has made a substantial impact on modern material research, making it suitable for the study of atomic structure, as modulated by strain, on the selected properties relating to anode performance.[29] For this study, the Vienna Ab Initio Simulation Package (VASP) was utilized, which is a DFT code that implements the projector-augmented-wave method to describe the electron-ion interaction.[30][31] Additionally, vaspkit was used to implement the electron-ion interactions.[32] For all simulated materials, initial structures were extracted from the publicly available resource Materials Project.[33] The initial structures of the 2D materials, extracted from Materials Project, were used to set up the pristine models. The models were then optimised through performing convergence tests and geometry optimization, guiding the choice of exchange-correlation functional. The strained models were attained through modulation of the pristine models. Subsequently, the vacancy formation energies, potassium adsorption energies, and electronic structures were calculated for the various models. For results relating to the vacancy formation and adsorption energy, spin polarization was taken into account.

2.1 Convergence tests

To assure the accuracy of the models, convergence tests were performed. The parameters that are set through the convergence tests include kpoints, plane wave cutoff energy, vacuum size and the supercell size. Provided that the parameters have resulted in a sufficiently converged model, they were set accordingly. In this case, increasing the parameters further, no longer leads to a significant change in total energy, thus excluding the necessity for higher values in light of computational cost.

K-points refer to the number of points that are used to sample the Brillouin zone, for which the Monkhorst-Pack scheme was used.[34] The vacuum size was increased and converged to ensure the accurate modeling of isolated 2D materials, as the periodic supercell is expanded in all directions. The convergence criterion chosen for the k-points, plane wave cutoff energy, and vacuum size was 0.01 eV/atom. Therefore, convergence was considered to be reached when increasing a parameter

no longer led to a significant change in total energy, defined as being greater than 0.01 eV/atom. For the geometry optimisations, the convergence criterion for the total energy of the system was aimed to be 0.1 eV. A maximum deviation of 0.1 Å from the pristine model was considered for the bond lengths at the edge of the supercell. However, due to time considerations, a general convergence criterion of 0.3 eV and deviation of 0.2 Å was chosen.

In addition to plane wave cutoff, k-points and vacuum size, the supercell size also needs to be converged, something that is especially important for the defective systems. As the supercell is expanded in all directions, its size needs to be sufficiently large to ensure the calculation of an isolated vacancy or adsorbed potassium atom. In this case, the modified supercell will not be affected by vacancies or adsorbed potassium atoms from neighboring supercells.

The convergence tests were performed on a unit cell for phosphorene and graphene. For silicene, a 2x2 cell was used. The k-points showed to be converged at 7x7x1, 33x33x1, and 11x1x11 for silicene, graphene, and phosphorene respectively. The plane wave cutoff energy was set at 400, 800 and 400 eV. For the vacuum size, values of 10 Å, 8 Å, and 20 Å were used.

For graphene and silicene, the supercell size was chosen to be an 8x8 cell containing 128 atoms. The supercell size for phosphorene was taken to be a 6x6 cell containing 144 atoms. Due to time considerations it was not considered feasible to go up to larger systems. Therefore, the supercell models do not fully concord with the aimed convergence criteria.

For silicene, the energy of the system converged to the aimed convergence criterion of 0.1 eV. However, the Si-Si bond lengths at the edge of the system deviated maximally 0.016 Å from those of the pristine model, which lies above the aimed 0.01 Å. The 8x8 model of silicene is considered to conform to convergence criteria to a great extent and is expected to yield accurate results. The supercell model of graphene gives rise to an energy converged to 0.17 eV, and C-C bond lengths having a maximal deviation of 0.015 Å. While both not conform to the ideal convergence criteria, the values are considered close to convergence, and relatively accurate results and trends are expected. The model of phosphorene deviated the most significantly from the aimed convergence criteria in terms of total energy, having converged to 0.29 eV. This is considered to be an important point of discussion relating to the results of the vacancy and adsorption energies of phosphorene. At the edges of the cell, the OC and OB bond lengths had a maximal deviation of 0.003 Å and 0.005 Å respectively. Therefore, the bond lengths at the edges do conform well to those of the pristine model. The graphs representing the results of the convergence tests can be found in Appendix A.

2.2 Choice of exchange-correlation functional

The exchange-correlation (XC) functional describes all the many-body interactions.[29] As there is no exact form for the XC functional to reach the answer for the ground state of the many-body Schrödinger equation, various approximations exist.[29] In this work, the XC functional was chosen to best describe the structural parameters of the 2D materials, as the effect of atomic structure, on anode performance, is studied.

The structure was assessed by evaluating structural parameters, such as bond lengths, bond angles, and lattice constants, of the models that were set up using various XC functionals. The 2x2 supercell models that were used were geometry optimized, where the positions of the atoms, the size and volume of the cell were allowed to relax until sufficient accuracy was reached. The required accuracy for all geometry optimizations was set at an energy difference of -10^{-2} eV. The ground state of the models were found for each of the considered XC functionals, including optPBE-vdW [35], vdW-DF/vdW-DF2 [36][37], PBE [38], PBEsol [39] and PBErev [40]. Van der Waals corrections were either included in the functionals or implemented by means of the DFT-D3 method.[41] The corrections were explicitly applied in calculations relating to the adsorption and vacancy formation energies. Particularly, they were of importance in the calculation of physical adsorption energies, as van der Waals interaction play an important role between the potassium atom and the surface.[42]

An appropriate choice of functional was based on the structural parameters of the models. The structure of the models was assessed through evaluating the structural parameters, for which the bond lengths and angles were determined by use of the atomic simulation environment (ASE).[43]

The parameters were compared to reference values, and the choice of XC functional was made for the models most closely fitting to the structure of the 2D materials as presented by the selected literature.

As a result, PBEsol was chosen as XC functional for each of the materials, resulting in models best conforming in structure to the 2D materials as presented by the selected literature (table 1). For graphene, experimental values of the structural parameters were used as a reference.[44][45] For silicene and phosphorene, computational studies were chosen as reference, which used LDA and SGGA-PBE as XC functionals respectively.[46][47]

The choice for XC functional was based on the maximal and average deviation of the calculated structural parameters from the chosen literature, which are shown in table 1. For silicene and graphene, PBEsol showed to be the best choice in respect to both the maximal and average deviation. In the case of phosphorene, the maximal deviation of various functionals were of the same range. Therefore, the lowest average deviation across the structural parameters was prioritized, thus resulting in the choice for PBEsol. The more detailed motivation behind the choice of XC functional can be found in Appendix B, comprising the values of the calculated and the referenced structural parameters along with the deviation.

Table 1: The average deviation and maximal deviation from the referenced literature for each material, taken over the calculated structural parameters (lattice constants, bond lengths, bond angles), shown in %, denoted by d_{avg} and d_{max} . Silicene, graphene, and phosphorene are denoted by Si, C, and P respectively.

	Si		C		P	
	d_{avg}	d_{max}	d_{avg}	d_{max}	d_{avg}	d_{max}
optPBE-VdW	1.12	1.64	0.28	0.42	2.06	5.48
PBE (+D3)	0.81	1.24	0.19	0.29	1.52	4.79
VdW-DF/VdW-DF2	1.72	2.49	0.46	0.70	3.31	8.22
revPBE (+D3)	1.22	1.60	0.41	0.63	1.53	4.67
PBEsol (+D3)	0.49	0.76	0.03	0.07	1.45	4.79

As a result of the choice of XC functionals, pristine models were obtained containing structures that compare to those of the selected reference studies. The resulting optimised structure of the pristine silicene model has a lattice constant of 3.847, a Si-Si bond length of 2.267 Å, and a Si-Si-Si bond angle of 116.1°. The structural parameters of the pristine graphene model show a lattice constant of 2.46 Å, a C-C bond length of 1.42 Å and a C-C-C bond angle of 120°. This model shows excellent agreement with experimental values, with a maximum deviation of 0.07 %. The lattice constant a and c of the pristine phosphorene model include 3.29 Å and 4.59 Å respectively. The OB and OC bond lengths had the respective values of 2.212 Å and 2.239 Å, while the AOB and BOC bond angles were determined to be 96.0° and 102.4°.

2.3 Setup of strained models

To evaluate the effect of strain as a means to increasing KIB anode performance, strained models were set up by modulating the pristine models that resulted from the convergence tests, geometry optimization, and choice of XC functional. Various strains were applied by multiplying the lattice vectors of the pristine models with percentages ranging from -30% to +30%. Typically for 2D materials, in-plane strains over 5% are considered to be large deformations.[48] Therefore, a relatively large range of biaxial strains was applied, gaining a broad overview of the effects of strain on the 2D materials, including propensity for breakage.

Each strained structure was geometry optimized, where the positions of the ions were allowed to relax, while the volume and size of the cell remained fixed. Therefore, the structures were relaxed, while fixing the effect of the strain. The effect of the strain was initially assessed by determining the total energy of the strained models. This showed the energy needed to strain the system and divert it from its ground state, represented by the minimum energy. Additionally, the structural parameters of the strained models were determined, providing insight into the ways the materials yield to the forced modulation of strain. The range of the strains was individually modified for each of the 2D materials, upon assessment of significant changes in structure or energy.

2.4 Vacancy formation energy

To assess the structural stability of the models upon the applied strain, the tendency to form vacancies was calculated. This was done through the calculation of the vacancy formation energy, referring to the energy that it is needed to form a vacancy defect under equilibrium conditions, and is defined by

$$E_{vf} = E_{defect} - E_{pristine} + E_a, \quad (1)$$

where E_{vf} represents the vacancy formation energy, E_{defect} the total energy of the defective model, $E_{pristine}$ the total energy of the pristine model, and E_a the total energy of an atom in the pristine model.[49] When the vacancy formation energy consists of a relatively low value, less energy is needed to form a vacancy defect such that the material would be more prone to the formation of vacancy defects and possibly to structural instability. The defective model was obtained by modifying a pristine model, by removing an atom, and performing a geometry optimization. In this geometry optimization, the positions of the atoms were allowed to relax, while the rest remained fixed. This allowed for an appropriate comparison between the pristine and defective model.

2.5 Adsorption energy

The efficient adsorption of potassium is an important metric for anodes in KIB batteries. This metric was assessed by the calculation of the adsorption energy as defined by the following equation:

$$E_A = E_{adsorbed} - E_{substrate} - E_K, \quad (2)$$

where E_A represents the adsorption energy, $E_{adsorbed}$ the energy of the model containing the adsorbed potassium, $E_{substrate}$ the total energy of the substrate model, and E_K the energy of an isolated potassium atom.[50] Negative adsorption energies are in the focus of this work the most favorable, as they correspond to a high affinity for adsorption.

For the calculation of the adsorption energies, the vacuum size of the models was increased with at least 7 Å to account for the added potassium. The potassium was added to various adsorption sites, with a distance from the surface of 2.5 Å. Similarly to the defective models, the models with adsorbed potassium atoms were geometry optimized, obtaining relaxed structures. The energy of a potassium atom in a KIB was approximated by the energy of an isolated potassium atom. This energy was calculated by performing a simulation for a potassium atom in a box with dimensions of 14 x 14 x 14 Å, allowing for the calculation on an isolated atom. For each of the materials, E_K was uniquely calculated with parameters corresponding to the respective models. The plane wave cutoff energy of the potassium atom was found to be converged for the values of the plane wave cutoff used for the models. The result of this convergence test can be found in Appendix A.

2.6 Bader charges

The Bader charges of various models were evaluated to better understand the systems that arise upon vacancy formation and potassium adsorption. The analysis was performed by means of the publicly available Bader Charge Analysis code as provided by the Henkelman group.[51] The analysis can provide a good approximation of the total electronic charge of an atom.[52] Therefore, calculating the Bader charge, provides a means to quantify charge redistribution and transfer processes such as vacancy formation and adsorption. For the formation of vacancy defects, the focus will be on how the charge is redistributed as bonds are no longer made with the vacant atom. Upon potassium adsorption, the potassium atom bonds with atoms on the 2D surface, resulting in a redistribution of charge. Therefore, the calculation of Bader charges can be used to better understand the interaction of vacancy defects and potassium atoms with the 2D surfaces. Specifically, the analysis will be done on the pristine models, and moreover Bader charges on selected strained models were calculated that showed a significant difference in adsorption or vacancy formation energy with respect to the pristine model.

2.7 Electronic properties

The conductivity of a material is of importance in its application as anode. Therefore, the density of states and band structures, as a proxy for electrical conductivity, were calculated for the pristine and strained models. For each of these models, the primitive cell was determined from the geometry optimized 2x2 supercell using vaspkit.[32] For the band structures, a high symmetry path along the Brillouin zone was taken. The coordinates of the high symmetry points were determined using SeekPath.[53][54] The density of states and band structures were plotted using py4vasp.[55] The projected density of states was obtained by use of vaspkit.[32]

3 Results

3.1 Pristine models

Throughout the research the pristine models were taken as a reference to evaluate the effect of strain in respect to the pristine models. The pristine models of a) graphene, b) silicene, and c) phosphorene, are represented in figure 4., showing the structural parameters of the models.

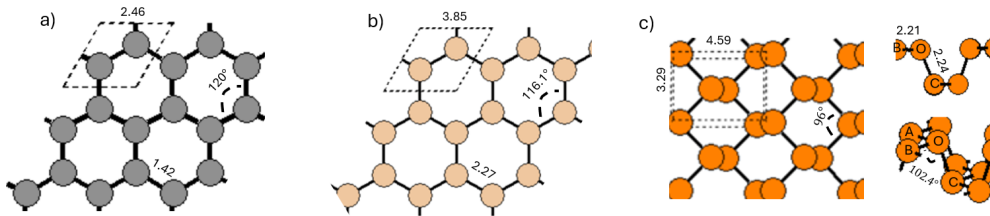


Figure 4: An illustration of the pristine models of a) graphene, b) silicene, and c) phosphorene, showing the values for the evaluated structural parameters.

To assess the change in electronic structure upon strain, the density of states and band structures were simulated for the optimised structures, with the pristine models taken as a reference. The electronic properties calculated for the pristine models were found to be in accordance with the literature.[56][57][58][59][60] For graphene and silicene, the density of states and the band structures showed the expected Dirac cones.[56][57][58] Phosphorene showed a bandgap of 0.65 eV, which is comparable to previously reported values in the literature (0.80/0.87 eV) considering different use of functional and simulation parameters.[59][60] Therefore, phosphorene was found to be semiconducting, in agreement with literature. The mentioned characteristics of the electronic properties are shown in the calculated density of states and band structures (figure 5).

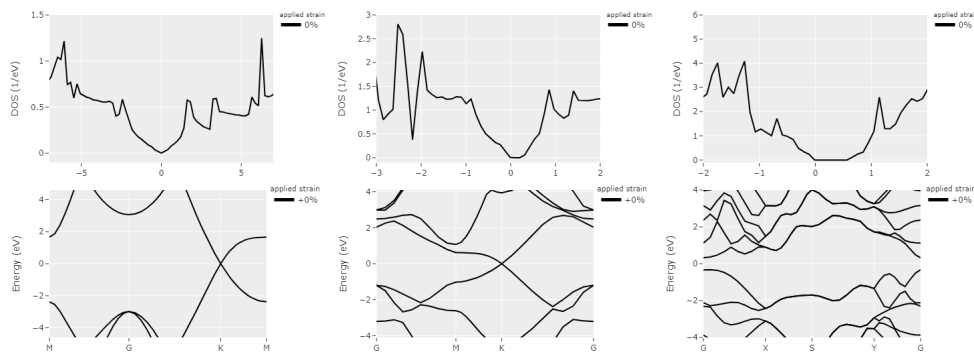


Figure 5: The density of states and band structures of the pristine models are shown for graphene, silicene, and phosphorene respectively. For graphene and silicene the characteristic Dirac cones are present, concurring with the literature. The density of states of phosphorene shows a bandgap as expected.

3.2 Strain engineering of undefective models

The strained models were initially assessed on energy and structure to determine the range of applicable strains, and moreover, to get an overview of the (electronic) structural changes, as modulated by strain, that affect the calculated properties relating to anode performance. In figure 6, the energy of the strained models are set out against the applied strain. This graph shows parabolic behavior for all three materials for the deviation from the ground state of the unstrained system. For silicene, the energy outside the range of -10% to +10% strains starts significantly deviating from the pristine system. Therefore, an initial range of strains between -10% and +10% was chosen to assess the effect of strain on silicene. As a result of the additional initial assessment on the structure of the strained models, a range of -5% to +20% was chosen for phosphorene. Outside the range of -5% to +25%, phosphorus atoms were found to make different bonds, resulting in notable differences with the structure of the pristine model, as shown in figure 7. In the rest of this work, the range of strains was chosen to be -5% to +10%, allowing for sufficient comparison between the compressed and tensile strained models. Overall, the results of the initial assessment of the strained models concord with the known structural stability and mechanical strength of the materials. For graphene, known as a strong material, no initial reassessment of the range of strains was considered, though for the significantly high compressive strains of -20% to -30% it should be noted that the carbon atoms started to make significantly more bonds, including bonds with carbon atoms outside of their nearest neighbors. In contrast, the range of strains for phosphorene and silicene was significantly reduced, for compressive as well as tensile strains, to a smaller range, corresponding to the respective structural instability and susceptibility to fracture formation.

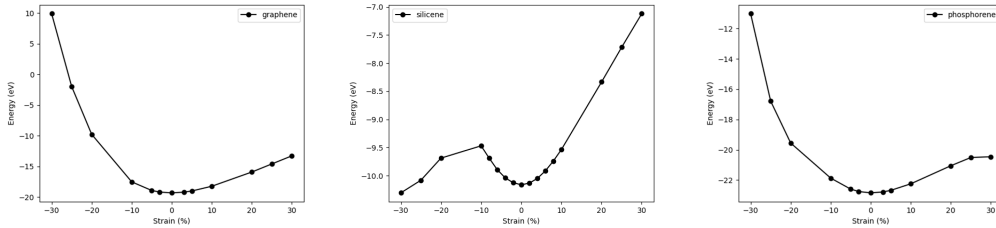


Figure 6: The energy of the strained models as a function of various applied strain.

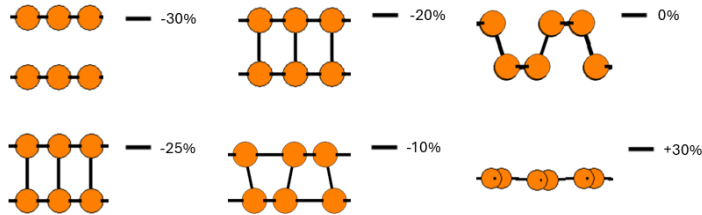


Figure 7: Various models of phosphorene shown outside of the range from -5% to +25% that resulted in structures significantly different from the pristine structure, which is additionally represented in the figure.

As shown in figure 6, the energy of the compressed models generally deviate more significantly from the ground state. For graphene, this is specifically shown for the strains ranging from 20% to 30%. Therefore, it is not surprising that upon geometry optimization of the respective supercells, the structures became significantly disordered. These models were therefore omitted in the calculations of the vacancy formation and adsorption energies. The ranges of strains for the models were further modified upon introduction of vacancy defects and potassium adsorption, resulting in bent or disordered structures for high applied strains.

3.2.1 Structural changes as a function of strain

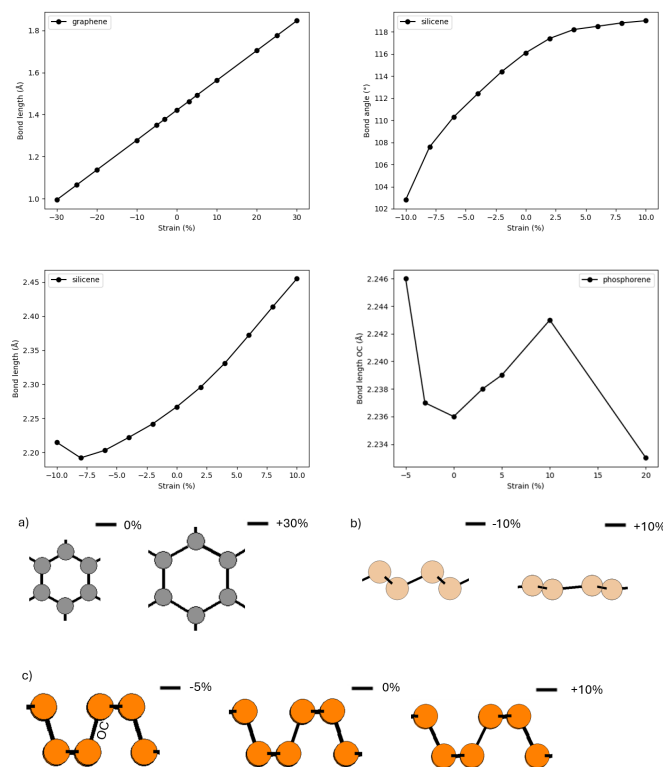


Figure 8: The change in structure upon strain represented by selected structural parameters for each material. The effect of strain on structural parameters is shown, on the bond length for graphene, the bond angle and length for silicene, and the OC bond length for phosphorene. For each of the materials, figures are shown illustrating the change in structure upon the applied strain for a) graphene, b) silicene, and c) phosphorene.

For each material, the change in structure upon the applied strain was assessed to understand how the materials yield to strain, and moreover, to understand the effect of the change in structure, as modulated by strain, on the evaluated properties relating to anode performance. In general, bond lengths were found to increase upon tensile strains and decrease for compressive strains, in concordance with expectations. However, each material showed to yield differently to the applied strain.

Graphene was found to have the most stable reaction to the applied strain, which aligns with graphene being a strong material. Phosphorene showed to have the least consistent response to the strain, which could possibly be explained by its highly buckled structure and variety in bond lengths and angles. The various responses are illustrated in figure 8 by a few representative structural parameters set out against the strain. The stable reaction of graphene to the applied strain can be found in the C-C-C bond angle remaining constant with applied strain, while the C-C bond length showed to change in a strictly linear manner.

The structural parameters of phosphorene show in general a relatively linear response to the applied strain. The unpredictable behavior of phosphorene is found for the OC bond lengths (Figure 4), which do not reveal a clear trend upon the applied strain, as shown in figure 8. The results of silicene show a relatively regular reaction to the strain in terms of structural parameters. However, a difference is observed for the response to compressive as opposed to tensile strains. The Si-Si-Si bond angle shows to be most prominently affected by the application of compressive strains, while the Si-Si bond length is more prone to change upon the application of tensile strains, which is shown in figure 8.

For silicene, the distance between the upper and lower Si atoms was additionally evaluated, to understand the change in puckering upon applied strain. The effect of strain on the defined

distance shows to be relatively linear, showing that the structure flattens upon the application of tensile strain, while upon compression the structure becomes increasingly more buckled. The flattening of the structure is illustrated in figure 8 in b), along with structural changes for a) graphene and c) phosphorene, showing the increase in C-C bond length for graphene, and the change in OC bond length and structure for phosphorene. An overview of all evaluated structural parameters upon application of strain can be found in Appendix C.

3.2.2 Electronic structure changes as a function of strain

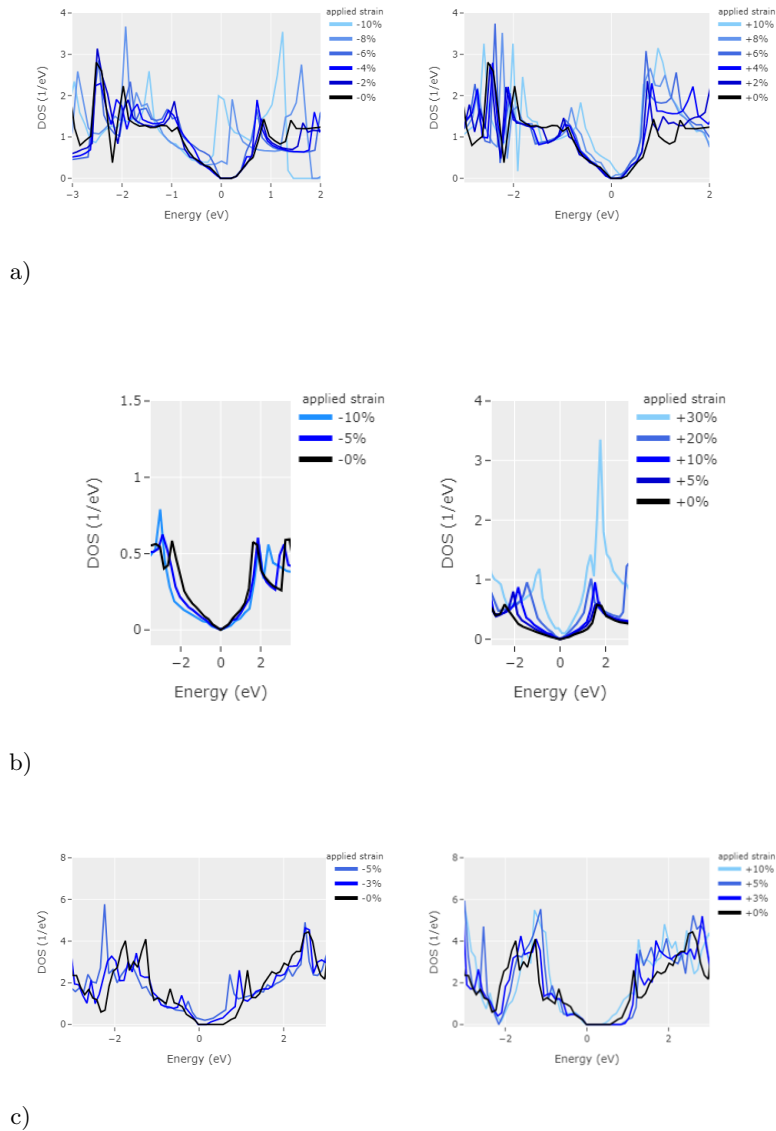


Figure 9: The change in density of states shown for a) silicene, b) graphene, and c) phosphorene, respectively, for various applied strains.

The change in electronic structure upon strain was evaluated as a proxy for electrical conductivity. The effect of the applied strain resulted in a different effect for each individual material. For silicene, the Dirac point was found to shift with applied strain (figure 9a) with the Dirac cone shifting to the valence band upon compressive strains and to the conduction band upon tensile

strains. In contrast, the Dirac cone of graphene changes in shape, becoming either steeper upon tensile strains, or broader upon compressive strains, which is shown in the calculated density of states in figure 9b. For phosphorene, which in contrast to graphene and silicene is a semiconductor, shows a direct correlation between band gap and applied strain. As shown in figure 10 the band gap becomes direct upon the 3% tensile strain. The band gap becomes smaller as the structure is compressed, likewise due to higher interactions between atoms that are forced closer together. The shrink of the band gap for the 10% tensile strain might be explained by the change in structure, where the structure is flattened (figure 8) resulting equally in more interaction between the atoms. This change in structure also served as a possible explanation for the sudden decline in adsorption energy for the 10% strained model, as presented in the results later on. The change in band gap can similarly be observed in the density of states shown in figure 9c. The calculated band structures for the various applied strains can be found in Appendix F.

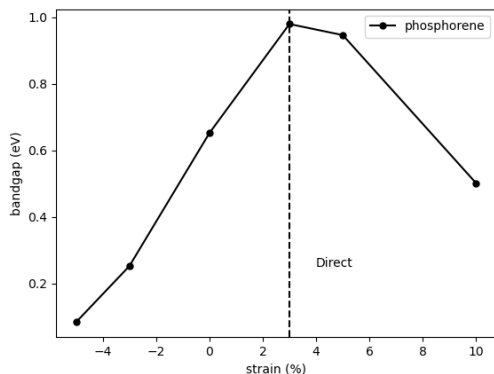


Figure 10: The band gap of phosphorene for various strains, where the band gaps for the tensile strains are direct.

In summary it was found that the energy, the structure, and electronic structure, significantly started deviating from the pristine models with applied strain. Changes in energy and structure resulted in a reassessment of the studied range of strains for each material, resulting in a range of -5% to +10% for graphene and phosphorene, and +2% to +10% for silicene. The effect of the strain as presented by the results show to concord with what is known about the mechanical strength and stability of the materials, showing graphene to have the most stable response to strain. The initial assessment on the change in (electronic) structure of the materials provides the basis for understanding the effect of strain as vacancy defects and potassium atoms are additionally introduced.

3.3 Vacancy strain engineering

The effect of strain engineering on the propensity of vacancy defect formation was assessed through the calculation of vacancy formation energies, with the pristine models taken as a reference. The values for the vacancy formation energy of pristine graphene, silicene, and phosphorene were calculated to be 7.70, 3.28 and 1.33 eV, respectively, in good agreement with previous literature.[49][61] The vacancies that resulted for a) graphene, b) silicene, and c) phosphorene, are represented in figure 11. With 7.70 eV as the highest calculated value, graphene shows to be the least prone to the formation of vacancy defects. This aligns with the known mechanical strength of graphene, adding to the mechanical strength that was previously found in the respective stable response to the application of strain. The relatively low vacancy formation energies for silicene and phosphorene correspond to their obstacles in KIB anode application, relating to structural instability.

Moreover, to understand the reorganisation of charge due to the introduction of a vacancy, the Bader charges were calculated to compare the pristine to the defective models (calculated Bader charges can be found in appendix G). For graphene, the charge transfer showed to be relatively delocalized. In the case of silicene, the atoms closest to the formed vacancy, showed to form four

bonds, instead of the common three, which can be found in the significant increase of charge (+0.173, +0.157, and +0.189) for these specific atoms. Moreover, it was found that atoms located farther away from the vacancy (about 2-3 bond lengths), still showed a significant change in charge due to the introduction of the vacancy defect. In the case of phosphorene, the atom located in the middle showed to have the most significant change in charge (-0.090), closest to the originally removed atom. This site was found to have a negative value (-0.064).

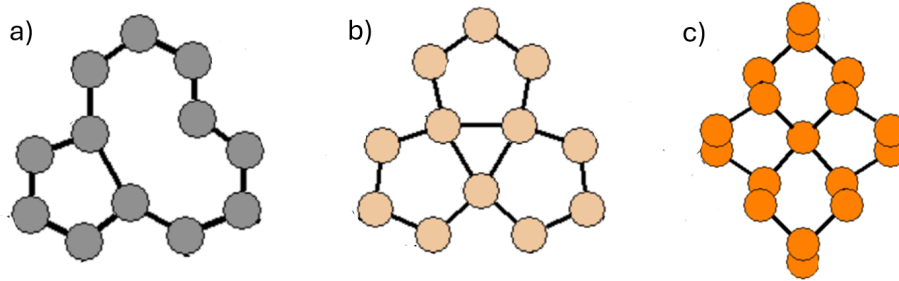


Figure 11: Vacancy defects in the defective models shown for a) graphene, b) silicene, and c) phosphorene.

It was found that upon the introduction of vacancy defects, the structural parameters changed in proximity. For silicene and graphene, both having hexagonal structures, it was found that the introduction of defects resulted in disordered structures for high strains. This is likely caused by additional strain that was induced by the introduction of defects, as illustrated by the generally found structural changes. As a result, the range of strains for silicene only consists of positive strains, as the compressed models resulted in bent or disordered structures. For the bent structures the vacancy formation energy was initially still calculated. However, it was found that the formation of vacancy defects significantly increased as can be seen in Appendix D. Additionally, the high tensile strained models of 20% and 30% of graphene showed to be significantly affected by the induced strain, resulting in under-coordinated carbon atoms. Therefore, the strained models that resulted in bent or disordered structures were omitted for silicene and graphene, resulting in only tensile strained models for silicene and a range from -5% to +10% for graphene for the calculation on the defective models. An example of models showing bent or disordered structures upon introduction of vacancy defects, can be found in figure 12.

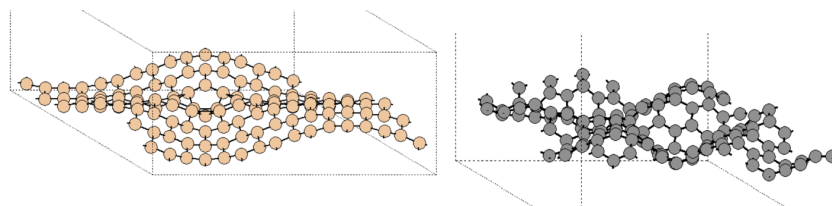


Figure 12: An example of the bent/disordered models arising as a result of vacancy defects for silicene (left) and graphene (right), respectively.

With the application of the reassessed strains, the likelihood of forming a vacancy defect changed, as shown for the three materials in figure 13. For compressive strains, the vacancy formation lowered, with 40.6% for graphene and 103.0% for phosphorene, showing an increased propensity for the formation of vacancy defects. This is in accordance with the previous results, showing that compressed strained models are more prone to significant structural changes and deformation. Tensile strains up to 5% or 6%, show vacancy formation energies that slightly increase with respect to the pristine model with a maximum increase of 0.6% for graphene, 14.9% for silicene, and 14.3% for phosphorene. For a high tensile strain of 10%, graphene and silicene show a significant decline in vacancy formation energy of 24.7% and 20.7% respectively, relative to the pristine models. This showed that it becomes more favorable to form defects as the system is

significantly tensile strained. This might point to a way for the hexagonal structure of silicene and graphene to release the energy of a significantly high applied tensile strain through the formation of a vacancy defect. This is additionally supported by the results for the highly tensile strained models of 20% and 30% for graphene, showing that uncoordinated carbon atoms formed upon the introduction of vacancies and potassium atoms.

With tensile strain, phosphorene shows a similar propensity to form vacancy defects in respect to the pristine model, even when a significant tensile strain of 10% is applied. The change in structure of the strained models resulted in a difference in the vacancies that formed, as illustrated in figure 14, where the vacancies of the pristine and 10% strained models are shown for a) graphene and b) silicene respectively, and for c) phosphorene the vacancies of the -5% strained and pristine model are shown. The calculated vacancy formation energies can be likewise found represented in tables in Appendix D, while calculated Bader charges for selected vacancies upon strain can be found in Appendix G.

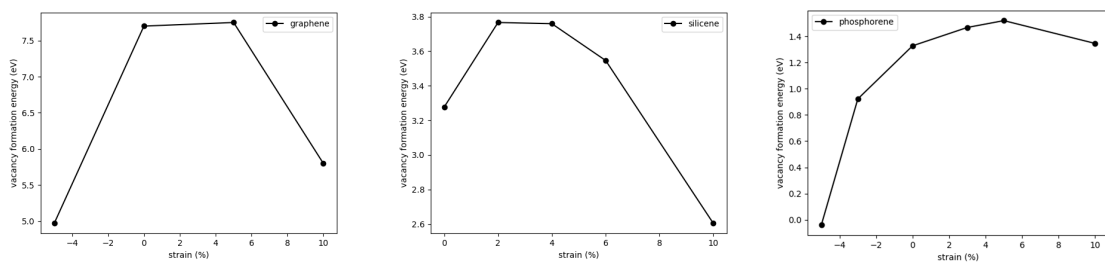


Figure 13: Vacancy formation energy as a function of strain for a) graphene, b) silicene, and c) phosphorene.

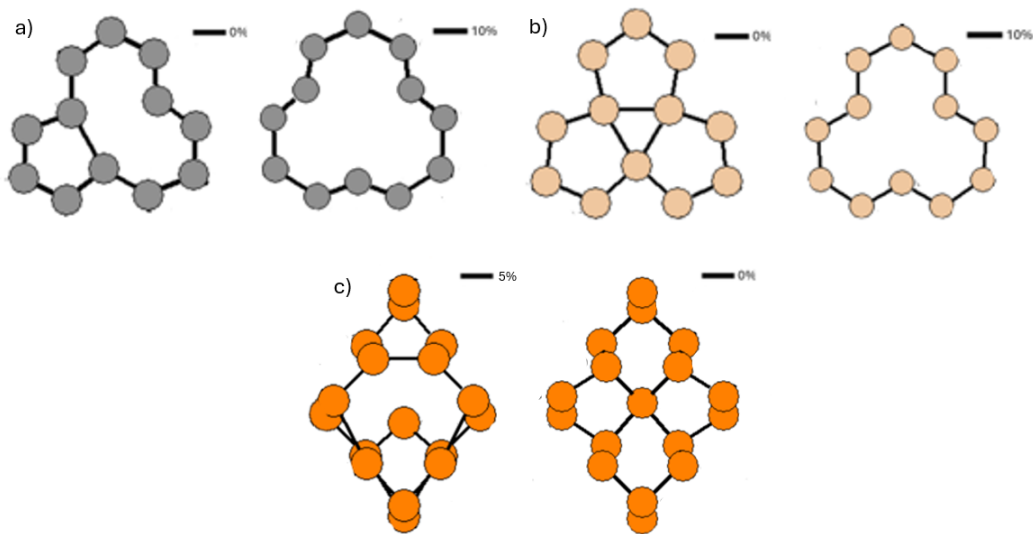


Figure 14: An illustration of the vacancies that formed for pristine and strained models for a) graphene, b) silicene, and c) phosphorene.

For selected defective models that showed to most deviate in vacancy formation energy in respect to the pristine models, the density of states were calculated. For graphene and silicene, the biggest deviation from the pristine density of states were found. For these materials, the Dirac cones were found to be distorted by the introduction of added peaks. The calculated density of states can be found in appendix F, showing the electronic structure for the defective pristine and strained models.

3.4 Potassium Adsorption

The calculation of the adsorption energy was used to assess the efficiency of potassium adsorption upon applied strain. Initially, the adsorption energy for the pristine models were calculated, to understand the changes that arise upon the application of strain. Potassium can adsorb onto various sites, hence that various sites were assessed to determine the most favorable site, referring to the site with the most negative value for the adsorption energy. The various sites that were assessed included the hole sites (H), top sites (T), and bridge sites (B), as shown in figure 15 for a) graphene, b) silicene, and c) phosphorene. The hole sites that were evaluated were taken to be the midpoint of the shown structures. Due to the puckering of silicene and phosphorene, additional sites were evaluated. For silicene, this included a distinction between the top sites on the upper and lower atoms, while for phosphorene a distinction was made between the upper and lower bridge sites. For each material, the most favorable site was found to be the H site which is in agreement with the literature, as shown in table 2. The adsorption energy of phosphorene shows to be the most negative with a value of -2.809 eV, which is followed by silicene and graphene respectively with the values of -2.190 eV and -1.80 eV. This is in agreement with the known values for the (theoretical) specific capacity for each of the materials, as the capacity of graphene is relatively low and the capacity for phosphorene was expected to be the highest. This shows that the calculation of the adsorption energy can be used as a good measure to evaluate potassium storage capacity in this research.

To understand the charge transfer upon the introduction of a potassium atom, the Bader charges were calculated to compare the pristine to the adsorbed models. For each material, the potassium adsorption showed to be ionic. The adsorption of potassium showed to be the most ionic for graphene. For graphene, the change in charge for the carbon atoms surrounding the H site was found to be delocalized. For silicene, this was likewise the case. However, it was shown that the upper atoms surrounding the H site had the most significant change in charge, gaining a more negative value. This is likely explained by the stronger formation of bonds formed with the upper atoms, relatively to the lower surface atoms of silicene. In the case of phosphorene, the transfer of charge likewise showed to be delocalized and in addition relatively symmetric. The calculated Bader charges for the pristine models, and the change in charge for the H sites containing adsorbed potassium, can be found in appendix G.

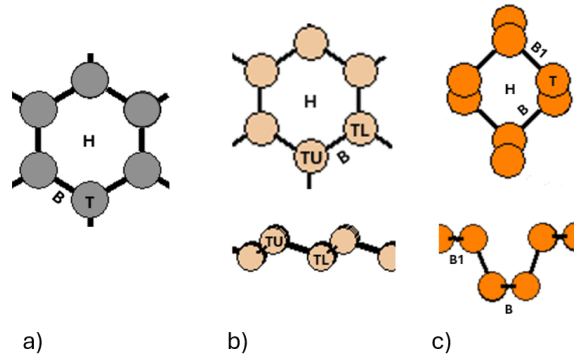


Figure 15: An illustration of the assessed adsorption sites of the pristine models of a) graphene, b) silicene, and c) phosphorene.

The adsorption energies that were calculated for the pristine models showed to be in good agreement with the referenced studies. This can be seen in table 2. The values of silicene, except for being slightly higher, show good agreement with the referenced study. The lower values of the referenced study could be explained by the omitted use of van der Waals corrections.[62] For graphene, the adsorption energies of the referenced study are considerably lower, which can be explained by the difference in use of functional.[50] A similar explanation for the relatively high values of phosphorene could be adopted, or could be partially ascribed to the relatively high convergence criterion for our supercell size.[63] For phosphorene, the T site was found to be unstable for

the methodology chosen in this work, therefore the T site is not included in table 2. The site was found unstable as the potassium atom moved away from the T site upon geometry optimization, when the positions of the atoms were allowed to relax. Overall, the adsorption energies are found to have similarity in value and in affinity of sites to the referenced studies.

Table 2: Adsorption energies of potassium on the pristine silicene, graphene, and phosphorene model respectively, compared to literature. The adsorption energies of silicene, graphene, and phosphorene are shown together with the distances $d_{K/Si}$, $d_{K/C}$, and $d_{K/P}$. Here, $d_{K/Si}$ (Å) is defined as the bond length between the adsorbed potassium atom and the nearest Si atom. For $d_{K/C}$ (Å) and $d_{K/P}$ (Å) the distance is defined as the separation between the adsorbed potassium atom and the surface layer.

E_A (eV)	TU	$d_{K/Si}$	TL	$d_{K/Si}$	H	$d_{K/Si}$	B	$d_{K/Si}$
Literature [62]	-1.704	3.18	-1.799	3.41	-2.188	2.91	-	-
Calculations	-2.068	3.19	-2.109	3.37	-2.190	3.49	-2.107	3.31

E_A (eV)	B	$d_{K/C}$	T	$d_{K/C}$	H	$d_{K/C}$
Literature [50]	-0.98	2.66	-0.98	2.68	-1.05	2.57
Calculations	-1.72	2.67	-1.72	2.69	-1.80	2.60

E_A (eV)	B	$d_{K/P}$	$B1$	$d_{K/P}$	H	$d_{K/P}$	T	$d_{K/P}$
Literature [63]	-	-	-0.940	-	-1.142	2.65	-0.554	-
Calculations	-2.783	2.52	-2.510	2.85	-2.809	2.53	-	-

3.4.1 Defective models

To understand the effect of introducing a vacancy defect onto a system, the adsorption energy was calculated on the unstrained defective models of the 2D materials. This was done by calculating the adsorption energy on various sites around the vacancy, and comparing these values to the adsorption energy on the reference sites, which were taken at edge of the supercell away from the vacancy defect. The various sites that were evaluated are shown in figure 16 for a) silicene, b) graphene, and c) phosphorene. Overall, the adsorption energy was found to strengthen when potassium is adsorbed near the vacancy, as opposed to sites on the edge of the cell. The strengthening of the adsorption energy at the most favorable site around the vacancy, in respect to the most favorable site on the edge of the cell, included 26% for graphene, 9% for silicene, and 12.7% for phosphorene. This points to the introduction of vacancy defects possibly contributing to potassium storage capacity.

For silicene, the adsorption energies on the edge were found to be between -2.83 and -2.99 eV, except for the TU site that was found to be unstable. With the chosen methodology, only the H1, H2 and H3 site around the vacancy were found to be stable, with the H2 site being the most favorable with a value for the adsorption energy of -3.26 eV. In the case of graphene, all sites on the edge were found to be stable, with a lowest adsorption energy of -2.03 eV. Around the vacancy, the B1 site was the only site that was found to be stable with an adsorption energy of -2.56 eV. At the edge of the phosphorene supercell only the H site was found to be stable, giving rise to an adsorption energy of -2.92 eV. The stable sites around the vacancy included the T1 and H2 site showing an increase in adsorption energy to -3.29 eV and -3.22 eV respectively. The T1 site was found to be the most favorable, likely relating to the found results for the Bader charges on the unstrained defective model of phosphorene. These results showed that the Bader charge of the T1 site significantly decreased due to the introduced vacancy, resulting in a significant negative value for this site, relative to surrounding atoms. The calculated adsorption energies for each unique adsorption site is included for each system in Appendix E.

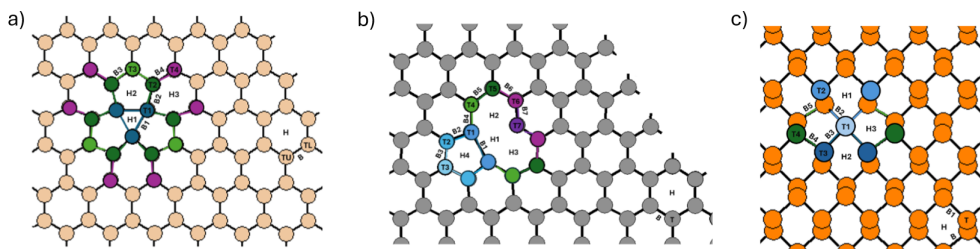


Figure 16: The evaluated adsorption sites labelled for the unstrained defective models of a) silicene, b) graphene and c) phosphorene.

3.4.2 Strain engineering

For the introduction of potassium atoms it was found that the structural parameters changed in proximity, likewise to the introduction of vacancy defects. For the strain engineering of potassium adsorption it was found that the structures of the highly strained models of silicene and graphene became bent or disordered, likely caused by additional strain induced by the potassium atom, likewise to the vacancy defects. For silicene, the adsorption energies on the bent structures were still calculated. However, it was found that the favorable adsorption sites significantly altered, as can be found in Appendix E. Therefore, the strained models that resulted in bent or disordered structures were omitted. This resulted in the omission of compressive strained models for silicene and graphene, and the higher tensile strained models of graphene for 20% and 30% applied strain. An example of models showing bent or disordered structures upon potassium adsorption, can be found in figure 17.

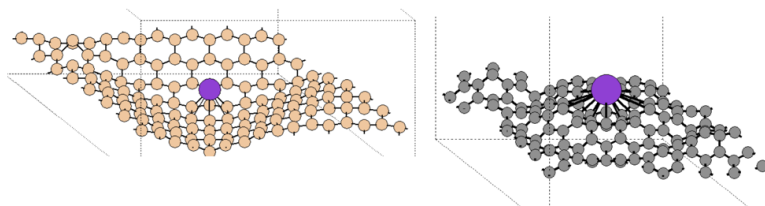


Figure 17: An example of the bent/disordered models arising as a result of potassium adsorption for silicene (left) and graphene (right), respectively.

The potassium adsorption was assessed for the resulting strained models. It was found that the adsorption energy changed due to application of strain for each of the 2D materials, as shown in figure 18. For each material, there are strained models that show an adsorption energy stronger to that of the pristine model. Specifically, for the 10% strained models each material shows a significant strengthening of adsorption energy of 36% for graphene, 32% for silicene and 12% for phosphorene. This shows that strain engineering could be an applicable method in the improving of potassium storage capacity for each of these materials.

The change in adsorption energies can likely be explained by the change in structure. The H sites were found to remain the most favorable for each material upon the application of strain. However, the characteristics of the hole sites changes through the modulation of the structures through strain. For graphene, as shown in a) in figure 19, the hole site increases upon strain, as expected based on previous results, possibly allowing the potassium atom to adsorb closer to the surface. For graphene, tensile strain results in a considerable linear strengthening of the adsorption energy. This possibly relates to the linear increase of the bond length (and constant bond angle) as shown in previous results, resulting in a consistent change of the character of the evaluated hole site.

For silicene and phosphorene a significant strengthening between the +5% and +10% model can be noticed. This might be explained by the flattening of the initially more buckled structures. In

the case of silicene, the flattening of the structure possibly allows for the formation of stronger bonds between the potassium atom and the lower surface atoms, increasing adsorption energy, and potassium capacity storage. The flattening of the structure, could likewise be an explanation of the strengthening in adsorption energy for phosphorene. However, the change in the character of phosphorene shows to be more variable, as the structural change to the applied strains showed to be more varied. The change in structure of the hole sites is likewise shown for b) silicene and c) phosphorene in figure 19. This shows that for the strain engineering of potassium adsorption capacity, the structure of each of the materials is of importance as it relates to the structure of the adsorption sites.

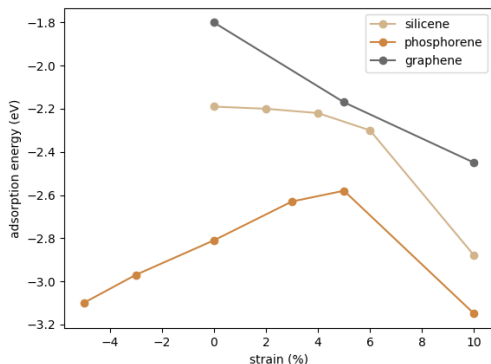


Figure 18: The adsorption energy of the H site shown against the various applied strains for the 2D materials.

The 10% tensile strained models of phosphorene, silicene, and graphene show the most significant strengthening of adsorption energy. However, the 10% tensile strained models of silicene and graphene were shown to be more prone to vacancy defect formation. This could additionally contribute to the improvement of potassium storage capacity, as shown by the previous results. However, if the formation of defects occurs in large quantities, this could likewise result in unstable structures. For silicene, this might be an issue as the lower vacancy formation energies for silicene and phosphorene showed to compare to their obstacles in application regarding mechanical strength and structural instability. In the case of graphene, the vacancy formation lowers to 5.80 eV, which is still significantly higher than the values for pristine silicene and phosphorene, hence the lower vacancy formation energy of graphene could additionally contribute to increasing potassium storage. For phosphorene, applying compressive strains might additionally be of use in increasing potassium storage. However, the vacancy formation energy showed to have a value of -0.04 eV, showing the formation of vacancy defects to be energetically favorable for this strained model in equilibrium conditions, which could hinder the use of compressive strains for phosphorene in KIB applications. The values of the adsorption energy upon strain for each of the evaluated sites and materials can be found in Appendix E. Additionally, the calculated Bader charges for the potassium atom and surrounding atoms for the strained models can be found in Appendix G.

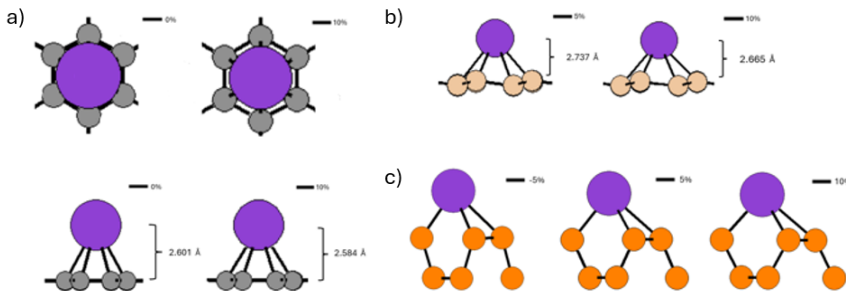


Figure 19: The change in potassium adsorption onto the H site upon applied strain is shown for a) graphene, b) silicene, and c) phosphorene.

3.4.3 Electronic structure

The projected density of states (PDOS) was calculated for selected models with adsorbed potassium that showed a significant change in adsorption energy with respect to the pristine models. The figures are included in Appendix F, and show in red the contribution of the potassium states to the conduction bands of the electronic structures of the materials. A higher contribution of potassium states to the conduction band likely points to a higher charge transfer from the potassium atom to the 2D materials. This is generally supported by the calculated Bader charges of the potassium atoms for the same systems. Considering the pristine models, the PDOS shows the smallest contribution of potassium states in the conduction band for phosphorene, followed by silicene and then graphene. This aligns with the adsorption of potassium onto the pristine phosphorene model being the least ionic and the most ionic for graphene. With strain, it is shown that the contribution of potassium states in the conduction shifts. For phosphorene, the contribution is the lowest for the 0% strained model, higher for the -5% and the highest for the 5% and 10% strained models. This additionally concords with the respective calculated Bader charges of 0.855, 0.856, 0.865 and 0.862. In the case of silicene, the contribution of the potassium states shows to increase between the 0% and 10% strained model, which shows a difference in regarding expectation relative to the respective Bader charges of 0.862 to 0.855. For graphene, the contribution shows to stay relatively the same between the 0% and 10% strained models, with respective Bader charges of 0.905 and 0.902. These results point at a high contribution of potassium states in the conduction band relating to a more ionic potassium adsorption. The mentioned results of the projected density of states, additionally with the calculated total density of states, of the adsorbed potassium systems can be found in Appendix F. The values for the Bader charges that were mentioned can be found in Appendix G.

Moreover, it was found that the potassium adsorption resulted in a decrease of the band gap for phosphorene across the various applied strains. This is represented by figure 20, and is important in the application of phosphorene as KIB anode, as potassium adsorption shows to increase electrical conductivity.

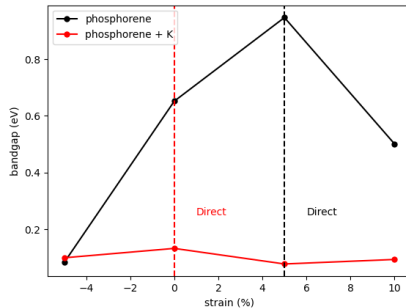


Figure 20: The bandgap of pristine phosphorene for various strains shown in comparison to the bandgap of phosphorene models with adsorbed potassium.

4 Conclusion

In this work, the effect of strain was evaluated on properties of 2D KIB anode materials, relating to anode performance, including the propensity to form vacancy defects, potassium adsorption energetics, and electronic structure. It was found that strain engineering is an applicable method that could be used in the enhancement of KIBs. In particular, this was found across the 2D anode materials for the +10% strained models, showing a significant strengthening of adsorption energy, pointing to an increase in potassium storage capacity. Additionally, it was found that the formation of vacancy defects could provide an additional means to improve potassium storage capacity, as the adsorption energy around the vacancy was shown to strengthen relative to states farther removed from the vacancy defect. In the application of strain engineering, tensile strains would be recommended over the use of compressive strains, as the compressive strained models showed overall to be more prone to significant structural changes and disorder.

Table 3: For each material, the strain of the strained model is shown that showed to contain the best prospects for KIB anode application, illustrated by the values for the vacancy formation energy and adsorption energy. The values for the pristine models are denoted in the brackets.

	+10% graphene	+6% silicene	+10% phosphorene
Vacancy formation energy (eV)	5.80 (7.70)	3.55 (3.28)	1.35 (1.33)
Adsorption energy (eV)	-2.45 (-1.80)	-2.30 (-2.19)	-3.15 (-2.81)

In table 3, the strained models that showed the best prospects for KIB anode application are shown for each of the materials. In brackets, the values of the pristine models are represented. As shown, the 10% tensile strained model was selected for graphene, as it shows a strengthening of adsorption energy in respect to the pristine model of 36.1%. Additionally, the vacancy formation energy lowered to a value of 5.80 eV, increasing the propensity to form vacancy defects, possibly allowing for an additional increase in potassium storage capacity. Therefore, the relatively low potassium storage capacity of pristine graphene is expected to significantly increase for the application of +10% tensile strain, resulting in comparable storage capacity to pristine silicene and phosphorene, selected for their high storage capacity. In the case of silicene, the +6% strained model showed to have the best prospects for KIB anode application. In respect to the adsorption energy, the +10% strained model showed the best prospects with a strengthening of adsorption energy with 32%. However, for this applied strain the vacancy formation energy was found to significantly decrease with 20.7% in respect to the pristine model. This would possibly result in a more significant obstacle in application of silicene as anode, regarding its susceptibility to form fractures. Therefore the +6% strain model was selected, showing a strengthening of adsorption energy with 5% and an increase in vacancy formation energy of 8.2%. Regarding phosphorene, the 10% strained model was selected showing a similar value in vacancy formation energy, a strengthening of the adsorption energy with 12.1%, and a decrease in band gap for pristine phosphorene of 23.1% improving electrical conductivity. However, it should be noted that the adsorption energy for phosphorene was found to be significantly stronger with a value of -3.15 eV, which could show to be an obstacle in KIB application, limiting potassium transport due to high affinity for potassium adsorption. Likewise, the strong adsorption energy could contribute to a significantly high storage capacity. In summary, the three selected strained models include 2D strained engineered material that show great promise in their application as KIB anodes, hence showing the applicability of strain engineering as a method to enhance KIB performance.

5 Future research

To further elucidate the general effect of strain across 2D anode materials, a wider variety of materials could be selected to better understand the effect of strain on materials showing a larger variety of (electronic) structures and composition. To gain a better understanding of the prospects of the 2D strain engineered materials in KIB application, the carrier mobility could be calculated to relate the change in electronic structure with strain, to the electrical conductivity of the materials. Additionally, the effect of strain on potassium storage capacity could be further elucidated through performing simulations to assess potassium adsorption for the introduction of multiple potassium atoms, in contrast to the study of the adsorption of an isolated potassium atom, more closely representing anode materials in the application of KIBs. Lastly, the effect of strain on 2D materials could be elucidated for a wider range of properties, focusing for example on other applications.

Acknowledgements

I would like to thank my supervisor Emilia Olsson for her guidance and help throughout the project. Additionally, I would like to express my gratitude to everyone in the Materials Theory and Modelling group for making me feel welcome and their willingness to answer any of my questions. Lastly, I would like to thank my family and friends for their support during the entirety of the project.

References

- [1] Shengxue Yang, Yujia Chen, and Chengbao Jiang. “Strain engineering of two-dimensional materials: Methods, properties, and applications”. In: *InfoMat* 3.4 (2021), pp. 397–420. DOI: <https://doi.org/10.1002/inf2.12177>. eprint: <https://onlinelibrary.wiley.com/doi/pdf/10.1002/inf2.12177>. URL: <https://onlinelibrary.wiley.com/doi/abs/10.1002/inf2.12177>.
- [2] J. Hao, J. Zheng, F. Ling, et al. “Strain-engineered two-dimensional MoS₂ as anode material for performance enhancement of Li/Na-ion batteries”. In: *Scientific Reports* 8 (2018), p. 2079. DOI: 10.1038/s41598-018-20334-z. URL: <https://doi.org/10.1038/s41598-018-20334-z>.
- [3] Maximilian Fichtner et al. “Rechargeable Batteries of the Future—The State of the Art from a BATTERY 2030+ Perspective”. In: *Advanced Energy Materials* 12.17 (2022), p. 2102904. DOI: <https://doi.org/10.1002/aenm.202102904>. eprint: <https://advanced.onlinelibrary.wiley.com/doi/pdf/10.1002/aenm.202102904>. URL: <https://advanced.onlinelibrary.wiley.com/doi/abs/10.1002/aenm.202102904>.
- [4] Ying Wu and Yan Yu. “2D material as anode for sodium ion batteries: Recent progress and perspectives”. In: *Energy Storage Materials* 16 (2019), pp. 323–343. ISSN: 2405-8297. DOI: <https://doi.org/10.1016/j.ensm.2018.05.026>. URL: <https://www.sciencedirect.com/science/article/pii/S2405829718304847>.
- [5] Mohammad Amir et al. “Energy storage technologies: An integrated survey of developments, global economical/environmental effects, optimal scheduling model, and sustainable adaption policies”. In: *Journal of Energy Storage* 72 (2023), p. 108694. ISSN: 2352-152X. DOI: <https://doi.org/10.1016/j.est.2023.108694>. URL: <https://www.sciencedirect.com/science/article/pii/S2352152X23020911>.
- [6] Meng Ma et al. “Advanced anode materials for potassium batteries: Sorting out opportunities and challenges by potassium storage mechanisms”. In: *Matter* 6.10 (2023), pp. 3220–3273. ISSN: 2590-2385. DOI: <https://doi.org/10.1016/j.matt.2023.07.009>. URL: <https://www.sciencedirect.com/science/article/pii/S2590238523003661>.
- [7] IEA. *The battery industry has entered a new phase*. IEA, Paris. Licence: CC BY 4.0. 2025. URL: <https://www.iea.org/commentaries/the-battery-industry-has-entered-a-new-phase>.
- [8] Naoki Nitta et al. “Li-ion battery materials: present and future”. In: *Materials Today* 18.5 (2015), pp. 252–264. ISSN: 1369-7021. DOI: <https://doi.org/10.1016/j.mattod.2014.10.040>. URL: <https://www.sciencedirect.com/science/article/pii/S1369702114004118>.
- [9] Yang Xu et al. “2023 roadmap for potassium-ion batteries”. In: *Journal of Physics: Energy* 5.2 (Apr. 2023), p. 021502. DOI: 10.1088/2515-7655/acbf76. URL: <https://dx.doi.org/10.1088/2515-7655/acbf76>.
- [10] Chenchen Zhang et al. “Progress and perspectives of 2D materials as anodes for potassium-ion batteries”. In: *Energy Storage Materials* 38 (2021), pp. 354–378. ISSN: 2405-8297. DOI: <https://doi.org/10.1016/j.ensm.2021.03.007>. URL: <https://www.sciencedirect.com/science/article/pii/S2405829721001057>.
- [11] Malvern Panalytical. *Battery Materials Characterization: Anode Materials*. <https://www.malvernpanalytical.com/en/industries/battery-and-energy-storage/battery-materials-characterization/anode-materials>. Accessed: 2025-05-26. 2025.
- [12] Zhiyuan Chen et al. “A comprehensive review of various carbonaceous materials for anodes in lithium-ion batteries”. In: *Dalton Transactions* 53.11 (2024), pp. 4900–4921. DOI: 10.1039/d3dt04010k.
- [13] Cristina Grosu et al. “Revisiting the Storage Capacity Limit of Graphite Battery Anodes: Spontaneous Lithium Overintercalation at Ambient Pressure”. In: *PRX Energy* 2 (1 Mar. 2023), p. 013003. DOI: 10.1103/PRXEnergy.2.013003. URL: <https://link.aps.org/doi/10.1103/PRXEnergy.2.013003>.

- [14] Xiaodan Li et al. “Graphite anode for potassium ion batteries: Current status and perspective”. In: *ENERGY and ENVIRONMENTAL MATERIALS* 5.2 (June 2021), pp. 458–469. DOI: 10.1002/eem2.12194.
- [15] Foysal Kabir Tareq and Souman Rudra. “Enhancing the performance of silicon-based anode materials for alkali metal (Li, Na, K) ion battery: A review on advanced strategies”. In: *Materials Today Communications* 39 (2024), p. 108653. ISSN: 2352-4928. DOI: <https://doi.org/10.1016/j.mtcomm.2024.108653>. URL: <https://www.sciencedirect.com/science/article/pii/S2352492824006342>.
- [16] Y.-M. Chang et al. “Two-dimensional materials as anodes for sodium-ion batteries”. In: *Materials Today Advances* 6 (2020), p. 100054. ISSN: 2590-0498. DOI: <https://doi.org/10.1016/j.mtadv.2020.100054>. URL: <https://www.sciencedirect.com/science/article/pii/S2590049820300011>.
- [17] Chandra Chowdhury, Sharmistha Karmakar, and Ayan Datta. “Capping Black Phosphorene by h-BN Enhances Performances in Anodes for Li and Na Ion Batteries”. In: *ACS Energy Letters* 1.1 (2016), pp. 253–259. DOI: 10.1021/acsenerylett.6b00164. eprint: <https://doi.org/10.1021/acsenerylett.6b00164>. URL: <https://doi.org/10.1021/acsenerylett.6b00164>.
- [18] Jakob Asenbauer et al. “The success story of graphite as a lithium-ion anode material – fundamentals, remaining challenges, and recent developments including silicon (oxide) composites”. In: *Sustainable Energy Fuels* 4 (11 2020), pp. 5387–5416. DOI: 10.1039/D0SE00175A. URL: <http://dx.doi.org/10.1039/D0SE00175A>.
- [19] Vestince B. Mbayachi et al. “Graphene synthesis, characterization and its applications: A review”. In: *Results in Chemistry* 3 (2021), p. 100163. ISSN: 2211-7156. DOI: <https://doi.org/10.1016/j.rechem.2021.100163>. URL: <https://www.sciencedirect.com/science/article/pii/S2211715621000680>.
- [20] C. Shen and S. Olutunde Oyadiji. “The processing and analysis of graphene and the strength enhancement effect of graphene-based filler materials: A review”. In: *Materials Today Physics* 15 (2020), p. 100257. ISSN: 2542-5293. DOI: <https://doi.org/10.1016/j.mtphys.2020.100257>. URL: <https://www.sciencedirect.com/science/article/pii/S254252932030081X>.
- [21] Keith Share et al. “Role of Nitrogen-Doped Graphene for Improved High-Capacity Potassium Ion Battery Anodes”. In: *ACS Nano* 10.10 (2016). PMID: 27718549, pp. 9738–9744. DOI: 10.1021/acsnano.6b05998. eprint: <https://doi.org/10.1021/acsnano.6b05998>. URL: <https://doi.org/10.1021/acsnano.6b05998>.
- [22] Foysal Kabir Tareq and Souman Rudra. “Enhancing the performance of silicon-based anode materials for alkali metal (Li, Na, K) ion battery: A review on advanced strategies”. In: *Materials Today Communications* 39 (2024), p. 108653. ISSN: 2352-4928. DOI: <https://doi.org/10.1016/j.mtcomm.2024.108653>. URL: <https://www.sciencedirect.com/science/article/pii/S2352492824006342>.
- [23] Rishabh Jain et al. “Reversible Alloying of Phosphorene with Potassium and Its Stabilization Using Reduced Graphene Oxide Buffer Layers”. In: *ACS Nano* 13.12 (2019). PMID: 31724845, pp. 14094–14106. DOI: 10.1021/acsnano.9b06680. eprint: <https://doi.org/10.1021/acsnano.9b06680>. URL: <https://doi.org/10.1021/acsnano.9b06680>.
- [24] A.Y. Galashev. “Prospects for using silicene as an anode for lithium-ion batteries. A review”. In: *Journal of Energy Storage* 93 (2024), p. 112281. ISSN: 2352-152X. DOI: <https://doi.org/10.1016/j.est.2024.112281>. URL: <https://www.sciencedirect.com/science/article/pii/S2352152X2401867X>.
- [25] Alexander Y. Galashev and Alexey S. Vorob’ev. “Physical properties of silicene electrodes for Li-, Na-, Mg-, and K-ion batteries”. In: *Journal of Solid State Electrochemistry* 22.11 (Nov. 2018), pp. 3383–3391. ISSN: 1433-0768. DOI: 10.1007/s10008-018-4050-8. URL: <https://doi.org/10.1007/s10008-018-4050-8>.

- [26] Lalla Btissam Drissi, Siham Sadki, and El Hassan Saidi. “Phosphorene: A 2D New Derivative of Black Phosphorous”. en. In: *Monoelements*. Ed. by Rajender Boddula Inamuddin, Mohd Imran Ahamed, and Abdullah M. Asiri. 1st ed. Wiley, Oct. 2020, pp. 1–26. ISBN: 9781119655251. DOI: 10.1002/9781119655275.ch1. URL: <https://onlinelibrary.wiley.com/doi/10.1002/9781119655275.ch1>.
- [27] Douglas C. Giancoli. *Physics for Scientists and Engineers*. 4th ed. See page 372. Upper Saddle River, NJ: Prentice Hall, 2008. ISBN: 9780132275590.
- [28] Zixin Xiong et al. “Structural Defects, Mechanical Behaviors, and Properties of Two-Dimensional Materials”. In: *Materials* 14.5 (2021). ISSN: 1996-1944. DOI: 10.3390/ma14051192. URL: <https://www.mdpi.com/1996-1944/14/5/1192>.
- [29] J. Hafner, C. Wolverton, and G. Ceder. “Toward Computational Materials Design: The Impact of Density Functional Theory on Materials Research”. In: *MRS Bulletin* 31 (2006), pp. 659–668. DOI: 10.1557/mrs2006.174. URL: <https://doi.org/10.1557/mrs2006.174>.
- [30] VASP Team. *About VASP*. <https://www.vasp.at/info/about/>. Accessed: 2025-05-27. 2024.
- [31] J. Hafner. “Materials simulations using VASP—a quantum perspective to materials science”. In: *Computer Physics Communications* 177.1 (2007). Proceedings of the Conference on Computational Physics 2006, pp. 6–13. ISSN: 0010-4655. DOI: <https://doi.org/10.1016/j.cpc.2007.02.045>. URL: <https://www.sciencedirect.com/science/article/pii/S001046550700080X>.
- [32] Wenxing Wang and Qingfeng Yin. “VASPkit: A user-friendly interface facilitating high-throughput computing and analysis using VASP code”. In: *Computer Physics Communications* 267 (2021), p. 108033. DOI: 10.1016/j.cpc.2021.108033.
- [33] Anubhav Jain et al. “The Materials Project: A materials genome approach to accelerating materials innovation”. In: *APL Materials* 1.1 (2013), p. 011002. DOI: 10.1063/1.4812323.
- [34] H. J. Monkhorst and J. D. Pack. “Special points for Brillouin-zone integrations”. In: *Physical Review B* 13.12 (1976), pp. 5188–5192. DOI: 10.1103/PhysRevB.13.5188.
- [35] Jiří Klimeš, David R Bowler, and Angelos Michaelides. “Chemical accuracy for the van der Waals density functional”. In: *Journal of Physics: Condensed Matter* 22.2 (Dec. 2009), p. 022201. DOI: 10.1088/0953-8984/22/2/022201. URL: <https://dx.doi.org/10.1088/0953-8984/22/2/022201>.
- [36] M. Dion et al. “Van der Waals Density Functional for General Geometries”. In: *Phys. Rev. Lett.* 92 (24 June 2004), p. 246401. DOI: 10.1103/PhysRevLett.92.246401. URL: <https://link.aps.org/doi/10.1103/PhysRevLett.92.246401>.
- [37] Kyuho Lee et al. “Higher-accuracy van der Waals density functional”. In: *Phys. Rev. B* 82 (8 Aug. 2010), p. 081101. DOI: 10.1103/PhysRevB.82.081101. URL: <https://link.aps.org/doi/10.1103/PhysRevB.82.081101>.
- [38] John P. Perdew, Kieron Burke, and Matthias Ernzerhof. “Generalized Gradient Approximation Made Simple”. In: *Phys. Rev. Lett.* 77 (18 Oct. 1996), pp. 3865–3868. DOI: 10.1103/PhysRevLett.77.3865. URL: <https://link.aps.org/doi/10.1103/PhysRevLett.77.3865>.
- [39] John P. Perdew et al. “Restoring the Density-Gradient Expansion for Exchange in Solids and Surfaces”. In: *Phys. Rev. Lett.* 100 (13 Apr. 2008), p. 136406. DOI: 10.1103/PhysRevLett.100.136406. URL: <https://link.aps.org/doi/10.1103/PhysRevLett.100.136406>.
- [40] Yingkai Zhang and Weitao Yang. “Comment on “Generalized Gradient Approximation Made Simple””. In: *Phys. Rev. Lett.* 80 (4 Jan. 1998), pp. 890–890. DOI: 10.1103/PhysRevLett.80.890. URL: <https://link.aps.org/doi/10.1103/PhysRevLett.80.890>.
- [41] Stefan Grimme et al. “A consistent and accurate ab initio parametrization of density functional dispersion correction (DFT-D) for the 94 elements H–Pu”. In: *The Journal of Chemical Physics* 132.15 (2010), p. 154104. DOI: 10.1063/1.3382344.

- [42] Jianmin Tao and Andrew M. Rappe. “Physical Adsorption: Theory of van der Waals Interactions between Particles and Clean Surfaces”. In: *Phys. Rev. Lett.* 112 (10 Mar. 2014), p. 106101. DOI: 10.1103/PhysRevLett.112.106101. URL: <https://link.aps.org/doi/10.1103/PhysRevLett.112.106101>.
- [43] Ask Hjorth Larsen et al. “The Atomic Simulation Environment—a Python library for working with atoms”. In: *Journal of Physics: Condensed Matter* 29.27 (2017), p. 273002. DOI: 10.1088/1361-648X/aa680e.
- [44] Jun-Wei Yang, Yanhong Yuan, and Guohong Chen. “First-principles study of potassium adsorption and diffusion on graphene”. In: *Molecular Physics* 118 (Feb. 2019), pp. 1–7. DOI: 10.1080/00268976.2019.1581291.
- [45] Alexander J. Bourque and Gregory C. Rutledge. “Empirical potential for molecular simulation of graphene nanoplatelets”. In: *The Journal of Chemical Physics* 148.14 (Apr. 2018), p. 144709. ISSN: 0021-9606. DOI: 10.1063/1.5023117. eprint: https://pubs.aip.org/aip/jcp/article-pdf/doi/10.1063/1.5023117/13551956/144709_1_online.pdf. URL: <https://doi.org/10.1063/1.5023117>.
- [46] H. Şahin et al. “Monolayer honeycomb structures of group-IV elements and III-V binary compounds: First-principles calculations”. In: *Physical Review B* 80.15 (Oct. 2009). ISSN: 1550-235X. DOI: 10.1103/physrevb.80.155453. URL: <http://dx.doi.org/10.1103/PhysRevB.80.155453>.
- [47] J. H. Huang, X. F. Wang, Y. S. Liu, et al. “Electronic Properties of Armchair Black Phosphorene Nanoribbons Edge-Modified by Transition Elements V, Cr, and Mn”. In: *Nanoscale Research Letters* 14 (2019), p. 145. DOI: 10.1186/s11671-019-2971-0. URL: <https://doi.org/10.1186/s11671-019-2971-0>.
- [48] Deji Akinwande et al. “A review on mechanics and mechanical properties of 2D materials—Graphene and beyond”. In: *Extreme Mechanics Letters* 13 (2017), pp. 42–77. ISSN: 2352-4316. DOI: <https://doi.org/10.1016/j.eml.2017.01.008>. URL: <https://www.sciencedirect.com/science/article/pii/S235243161630236X>.
- [49] Biswas Rijal et al. “Charged vacancy defects in monolayer phosphorene”. In: *Phys. Rev. Mater.* 5 (12 Dec. 2021), p. 124004. DOI: 10.1103/PhysRevMaterials.5.124004. URL: <https://link.aps.org/doi/10.1103/PhysRevMaterials.5.124004>.
- [50] Emilia Olsson et al. “Adsorption and migration of alkali metals (Li, Na, and K) on pristine and defective graphene surfaces”. In: *Nanoscale* 11 (12 2019), pp. 5274–5284. DOI: 10.1039/C8NR10383F. URL: <http://dx.doi.org/10.1039/C8NR10383F>.
- [51] URL: <https://theory.cm.utexas.edu/henkelman/code/bader/>.
- [52] URL: <https://henkelmanlab.org/research/bader/>.
- [53] Yoyo Hinuma et al. “Band structure diagram paths based on crystallography”. In: *Computational Materials Science* 128 (2017), pp. 140–184. DOI: 10.1016/j.commatsci.2016.10.015.
- [54] Atsushi Togo and Isao Tanaka. *Spglib: a software library for crystal symmetry search*. 2018. arXiv: arXiv:1808.01590 [cond-mat.mtrl-sci]. URL: <https://arxiv.org/abs/1808.01590>.
- [55] py4vasp developers. *py4vasp: A Python interface for VASP*. <https://www.vasp.at/py4vasp/latest/index.html>. 2024.
- [56] M Klintonberg et al. “Evolving properties of two-dimensional materials: from graphene to graphite”. In: *Journal of Physics: Condensed Matter* 21.33 (July 2009), p. 335502. DOI: 10.1088/0953-8984/21/33/335502. URL: <https://dx.doi.org/10.1088/0953-8984/21/33/335502>.
- [57] Ryan Newson. “Dynamics of Carriers and Photoinjected Currents in Carbon Nanotubes and Graphene”. In: (Jan. 2010).
- [58] Rong Wang et al. “Silicene oxides: formation, structures and electronic properties”. In: *Scientific Reports* 3.1 (Dec. 2013), p. 3507. ISSN: 2045-2322. DOI: 10.1038/srep03507. URL: <https://doi.org/10.1038/srep03507>.

- [59] S J Ray, M Venkata Kamalakar, and R Chowdhury. “Ab initio studies of phosphorene island single electron transistor”. In: *Journal of Physics: Condensed Matter* 28.19 (Apr. 2016), p. 195302. DOI: 10.1088/0953-8984/28/19/195302. URL: <https://dx.doi.org/10.1088/0953-8984/28/19/195302>.
- [60] Vadym Kulish et al. “Adsorption of Metal Adatoms on Single-Layer Phosphorene”. In: *Physical Chemistry Chemical Physics* 17 (Nov. 2014). DOI: 10.1039/C4CP03890H.
- [61] Muhammad Ali et al. “Electronic and magnetic properties of graphene, silicene and germanene with varying vacancy concentration”. In: *AIP Advances* 7.4 (Apr. 2017), p. 045308. ISSN: 2158-3226. DOI: 10.1063/1.4980836. eprint: https://pubs.aip.org/aip/adv/article-pdf/doi/10.1063/1.4980836/13096396/045308_1_online.pdf. URL: <https://doi.org/10.1063/1.4980836>.
- [62] Xianqing Lin and Jun Ni. “Much stronger binding of metal adatoms to silicene than to graphene: A first-principles study”. In: *Phys. Rev. B* 86 (7 Aug. 2012), p. 075440. DOI: 10.1103/PhysRevB.86.075440. URL: <https://link.aps.org/doi/10.1103/PhysRevB.86.075440>.
- [63] A. Sibari, Z. Kerrami, A. Kara, et al. “Adsorption and diffusion on a phosphorene monolayer: a DFT study”. In: *Journal of Solid State Electrochemistry* 22.1 (2018), pp. 11–16. DOI: 10.1007/s10008-017-3703-3. URL: <https://doi.org/10.1007/s10008-017-3703-3>.

Appendix A: Convergence Tests

Silicene

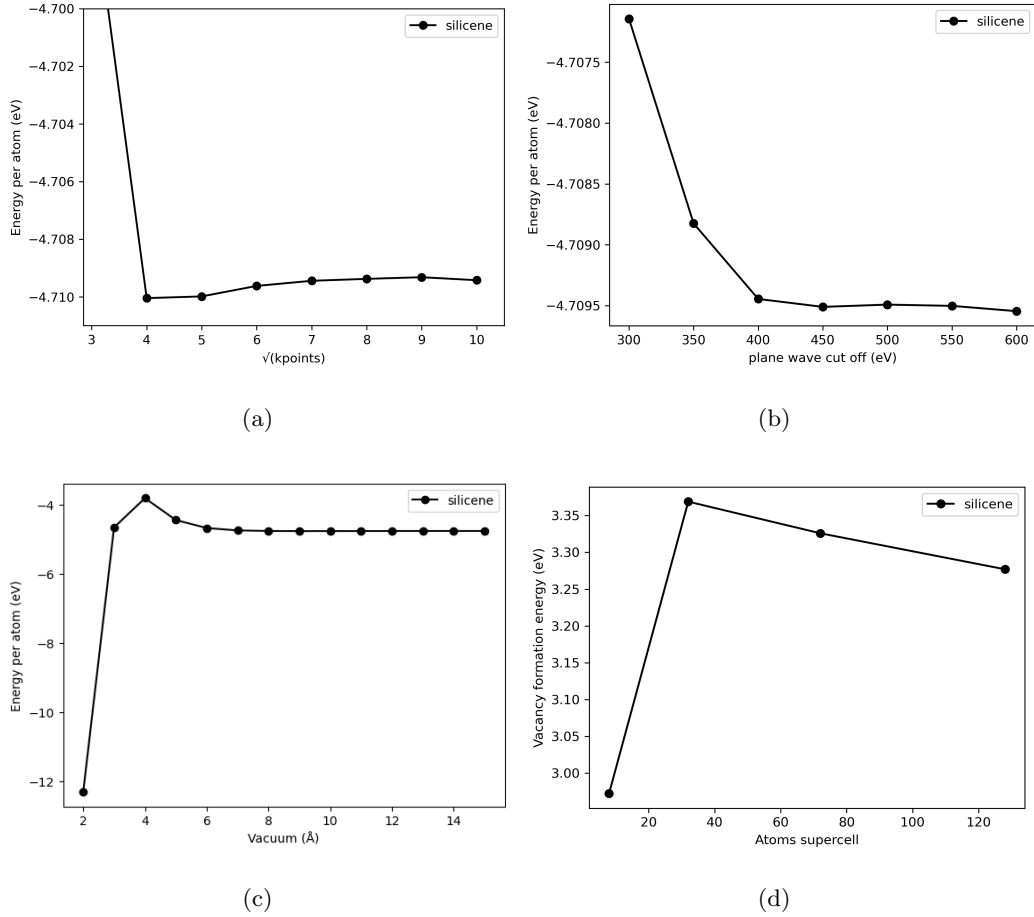


Figure 21: Convergence tests performed for silicene with PBE+D3 as XC functional: a. kpoints convergence test where the system was converged at $7 \times 7 \times 1$ for a convergence criterion of 0.01 eV/atom, b. plane wave cutoff energy convergence test where the system was converged at 400 eV for a convergence criterion of 0.01 eV/atom, c. vacuum convergence test where the system was converged at 10 \AA for a convergence criterion of 0.01 eV/atom, d. supercell size convergence test on the vacancy formation energy, where the system chosen was the 8×8 supercell which converged to 0.1 eV, below the general convergence criterion of 0.3 eV taken for the supercell size convergence test.

Graphene

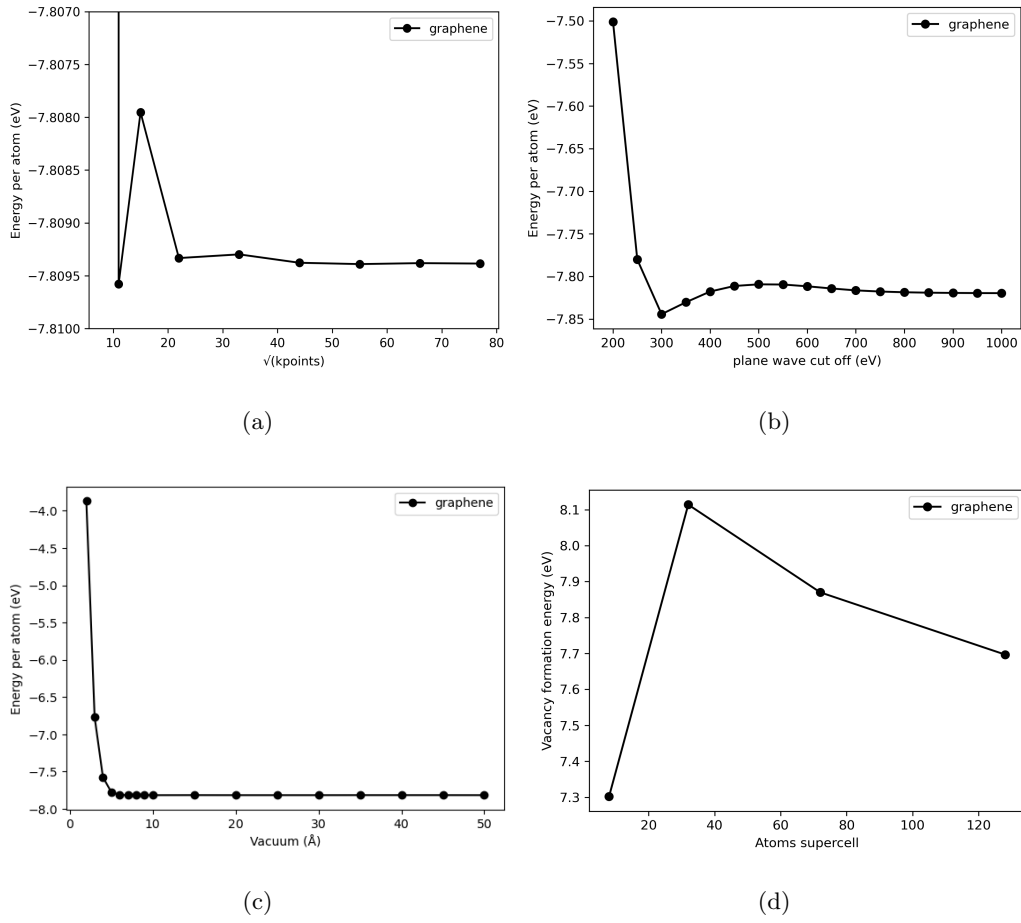


Figure 22: Convergence tests performed for graphene with optPBE-vdW as XC functional: a. kpoints convergence test where the system was converged at $33 \times 33 \times 1$ for a convergence criterion of 0.01 eV/atom, b. plane wave cutoff energy convergence test where the system was converged at 800 eV for a convergence criterion of 0.01 eV/atom, c. vacuum convergence test where the system was converged at 8 \AA for a convergence criterion of 0.01 eV/atom, d. supercell size convergence test on the vacancy formation energy, where the system chosen was the 8×8 supercell which converged to 0.18 eV, below the general convergence criterion of 0.3 eV taken for the supercell size convergence test.

Phosphorene

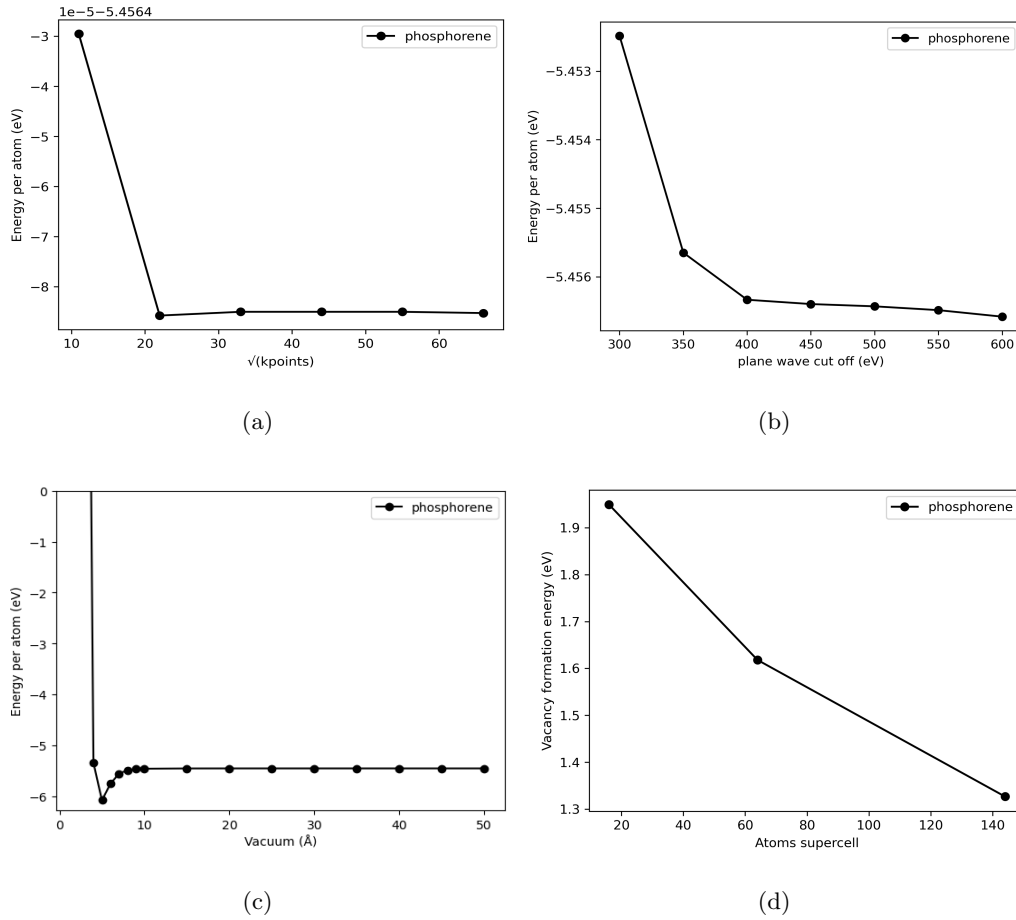


Figure 23: Convergence tests performed for phosphorene with PBE+D3 as XC functional: a. kpoints convergence test where the system was converged at $11 \times 11 \times 11$ for a convergence criterion of 0.01 eV/atom, b. plane wave cutoff energy convergence test where the system was converged at 400 eV for a convergence criterion of 0.01 eV/atom, c. vacuum convergence test where the system was converged at 20 \AA for a convergence criterion of 0.01 eV/atom, d. supercell size convergence test on the vacancy formation energy, where the system chosen was the 6×6 supercell which converged to 0.3 eV at the taken convergence triterium for the supercell size convergence test.

Potassium

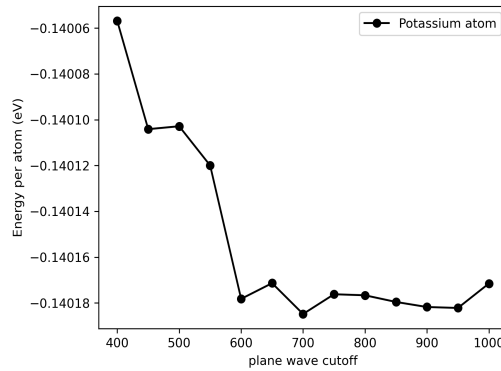


Figure 24: Convergence tests performed for an isolated potassium atom using PBE as XC functional, where it is shown that the plane wave cutoff energy is converged at 400 eV.

Appendix B: Structural Parameters

Silicene

Table 4: Structural properties of silicene for various XC functionals.. The structural parameters are shown with the respective deviation (dev) to the referenced literature. The lattice constant is denoted by a , the bond length by d and the bond angle by θ

	a (Å)	dev (%)	d (Å)	dev (%)	θ (°)	dev (%)
Literature [46]	3.83	-	2.25	-	116.4	-
optPBE-VdW	3.873	1.12	2.287	1.64	115.7	0.60
PBE+D3	3.866	0.94	2.278	1.24	116.1	0.26
VdW-DF2	3.899	1.80	2.306	2.49	115.4	0.86
revPBE+D3	3.882	1.36	2.286	1.60	116.2	0.71
PBEsol+D3	3.847	0.44	2.267	0.76	116.1	0.26

Graphene

Table 5: Structural properties of graphene for various XC functionals. The structural parameters are shown with the respective deviation (dev) to the referenced literature. The lattice constant is denoted by a , the bond length by d and the bond angle by θ .

	a (Å)	dev (%)	d (Å)	dev (%)	θ (°)	dev (%)
Literature [44][45]	2.46	-	1.42	-	120	-
optPBE-VdW	2.4702	0.41	1.426	0.42	120	0
PBE	2.4671	0.29	1.424	0.28	120	0
VdW-DF	2.4764	0.67	1.430	0.70	120	0
revPBE	2.4751	0.61	1.429	0.63	120	0
PBEsol	2.4604	0.02	1.421	0.07	120	0

Phosphorene

Table 6: Structural properties of phosphorene for various XC functionals.. The structural parameters are shown with the respective deviation (dev) to the referenced literature. The lattice constants are denoted by a and c , the bond lengths by d and the bond angles by θ

	a (Å)	dev (%)	c (Å)	dev (%)	d_{OB} (Å)	dev (%)	d_{OC} (Å)	dev (%)
Literature [47]	3.31	-	4.38	-	2.22	-	2.24	-
optPBE-VdW	3.32	0.30	4.62	5.48	2.237	0.77	2.278	1.70
PBE+D3	3.30	0.30	4.59	4.79	2.218	0.09	2.260	0.89
VdW-DF	3.35	1.21	4.74	8.22	2.248	1.26	2.297	2.54
revPBE+D3	3.31	0	4.67	4.67	2.222	0.09	2.270	1.34
PBEsol+D3	3.29	0.60	4.59	4.79	2.212	0.36	2.239	0.04

	θ_{AOB} (°)	dev (%)	θ_{BOC} (°)	dev (%)
Literature [47]	96.34	-	102.10	-
optPBE-VdW	95.9	0.46	103.8	1.67
PBE+D3	96.0	0.35	103.9	1.76
VdW-DF	96.2	0.15	104.6	2.45
revPBE+D3	96.3	0.04	104.5	2.35
PBEsol+D3	96.0	0.35	102.4	0.29

Appendix C: Strain engineering

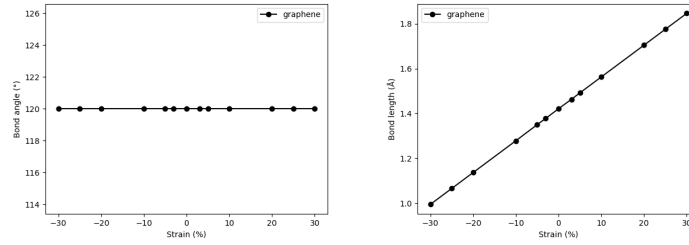


Figure 25: The change in bond angle, length, and distance shown against the various applied strains for graphene.

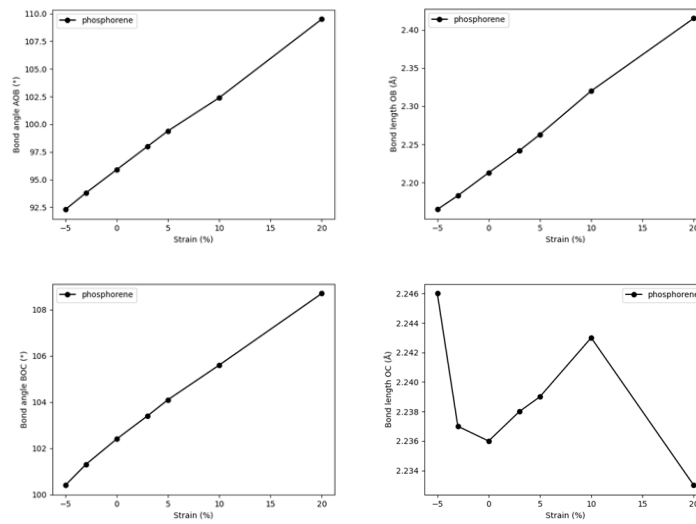


Figure 26: The change in bond lengths and angles for phosphorene shown against the various applied strains.

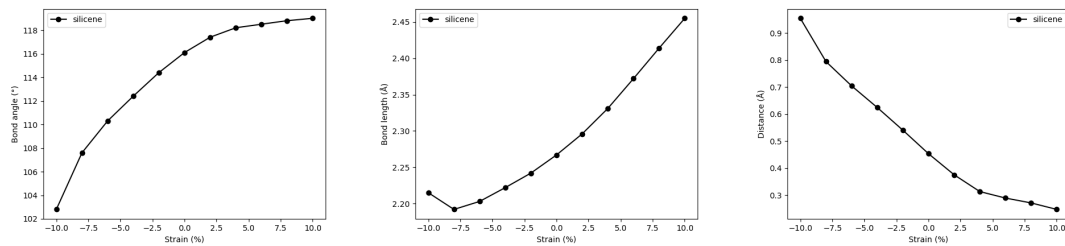


Figure 27: The change in bond angle, length, and distance shown against the various applied strains for silicene.

Appendix D: Vacancy formation energy

Silicene

Table 7: Vacancy formation energy (VFE) for various applied strains.

Strain (%)	VFE (eV)
-4	-4.05
-2	1.08
0	3.28
+2	3.77
+4	3.76
+6	3.55
+10	2.60

Graphene

Table 8: Vacancy formation energy (VFE) for various applied strains.

Strain (%)	VFE (eV)
-5	4.97
0	7.70
+5	7.75
+10	5.80

Phosphorene

Table 9: Vacancy formation energy (VFE) for various applied strains.

Strain (%)	VFE (eV)
-5	-0.04
-3	0.92
0	1.33
+3	1.47
+5	1.52
+10	1.35

Appendix E: Adsorption energy

Silicene

Table 10: Adsorption energy for the various sites of the strained models.

Strain (%)	<i>H</i>	<i>TU</i>	<i>TL</i>	<i>B</i>
-4	-6.91	-7.23	-7.07	-7.21
-2	-2.39	-3.20	-2.53	-3.14
+0	-2.19	-2.07	-2.11	-2.11
+2	-2.20	-2.06	-2.11	-
+4	-2.22	-2.07	-2.11	-
+6	-2.30	-2.15	-2.18	-
+10	-2.88	-2.68	-2.73	-2.72

Table 11: Adsorption energies of potassium for various sites on the unstrained defective model of silicene.

	<i>TL</i>	<i>T1</i>	<i>H</i>	<i>H1</i>	<i>H2</i>	<i>H3</i>	<i>B</i>
E_A (eV)	-2.829	-3.197	-2.987	-2.713	-3.256	-3.146	-2.906

Graphene

Table 12: Adsorption energy for the various sites of the strained models

Strain (%)	<i>H</i>	<i>T</i>	<i>B</i>
+0	-1.80	-1.72	-1.72
+5	-2.17	-2.09	-2.09
+10	-2.45	-2.36	-2.37

Table 13: Adsorption energies of potassium for various sites on the unstrained defective model of silicene.

	<i>T</i>	<i>H</i>	<i>B</i>	<i>B1</i>
E_A (eV)	-1.96	-2.03	-1.97	-2.56

Phosphorene

Table 14: Adsorption energy for the various sites of the strained models

Strain (%)	<i>H</i>	<i>B1</i>	<i>B</i>
-5	-3.10	-2.78	-3.02
-3	-2.97	-2.68	-2.94
+0	-2.81	-2.51	-2.78
+3	-2.63	-2.33	-2.61
+5	-2.58	-2.27	-2.55
+10	-3.15	-2.84	-3.12

Table 15: Adsorption energies of potassium for various sites on the unstrained defective model of phosphorene.

	<i>T1</i>	<i>H</i>	<i>H2</i>
E_A (eV)	-3.291	-2.921	-3.224

Appendix F: Electronic structure

Band structures: Strained models

Silicene

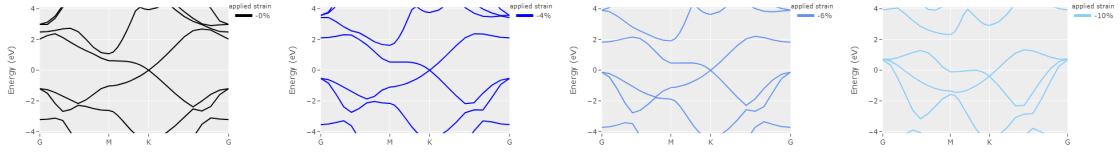


Figure 28: The band structures plotted for various compressive strains

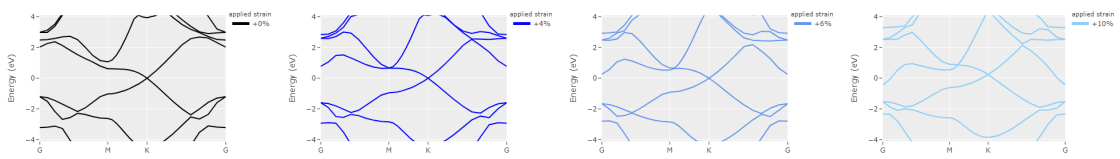


Figure 29: The band structures plotted for various tensile strains

Graphene

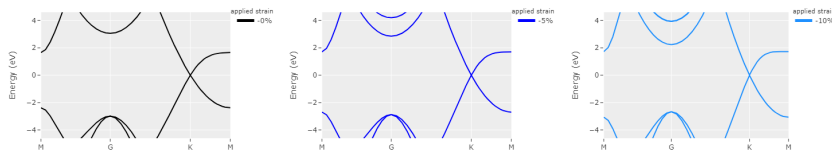


Figure 30: The band structures plotted for various compressive strains

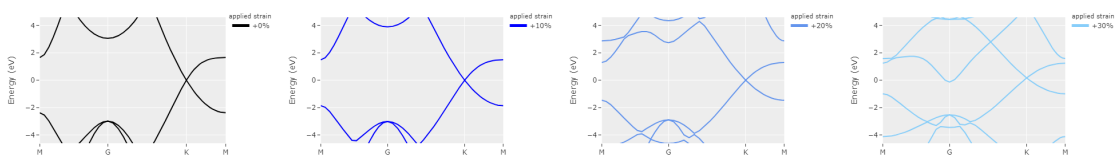


Figure 31: The band structures plotted for various tensile strains

Phosphorene

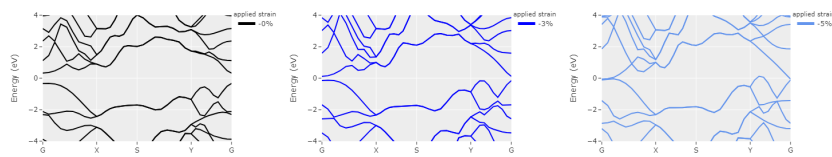


Figure 32: The band structures plotted for various compressive strains

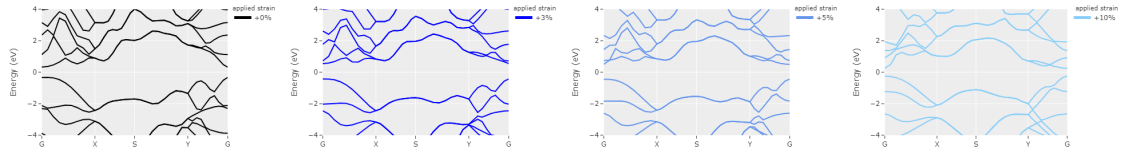


Figure 33: The band structures plotted for various tensile strains

Density of states: Vacancy defects

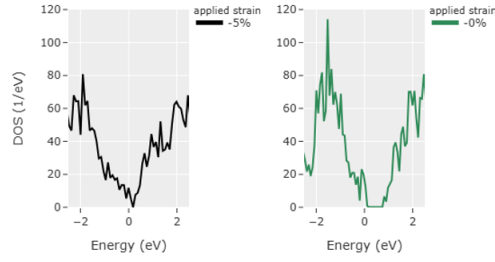


Figure 34: The total density of states shown for defective phosphorene for the -5% and 0% strained model.

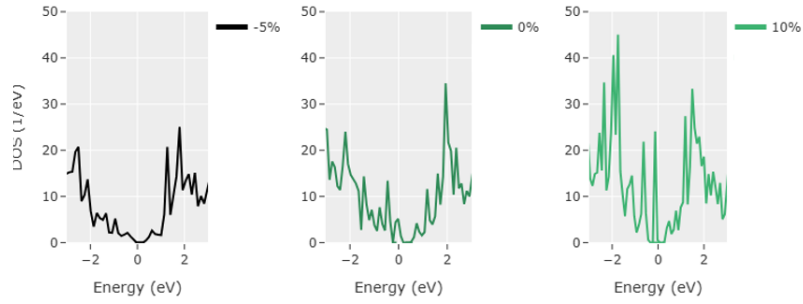


Figure 35: The total density of states shown for defective graphene for the -5%, 0% and 10% strained model.

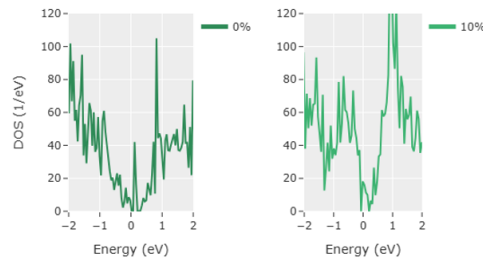


Figure 36: The total density of states shown for defective silicene for the 0% and 10% strained model.

Density of states: Potassium adsorption

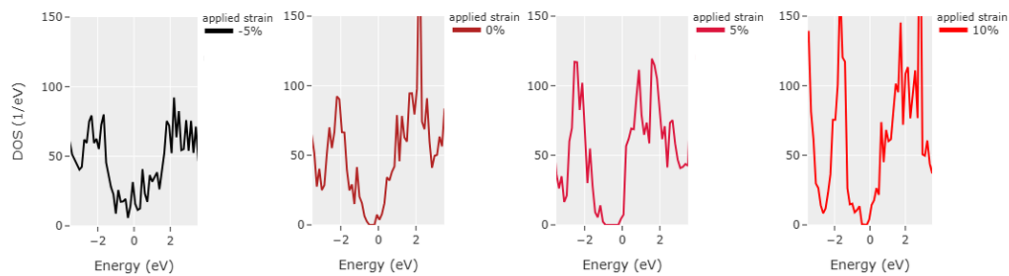


Figure 37: The total density of states shown for phosphorene with an adsorbed potassium atom on the H site for the -5%, 0%, 5% and 10% strained model.

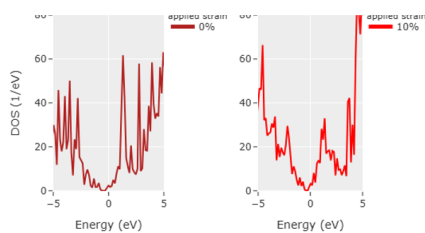


Figure 38: The total density of states shown for graphene with an adsorbed potassium atom on the H site for the 0% and 10% strained model.

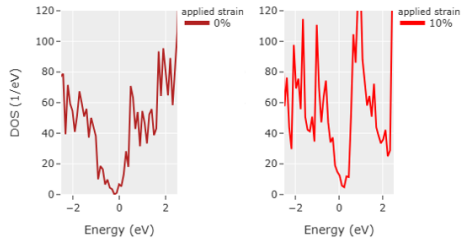


Figure 39: The total density of states shown for silicene with an adsorbed potassium atom on the H site for the 0% and 10% strained model.

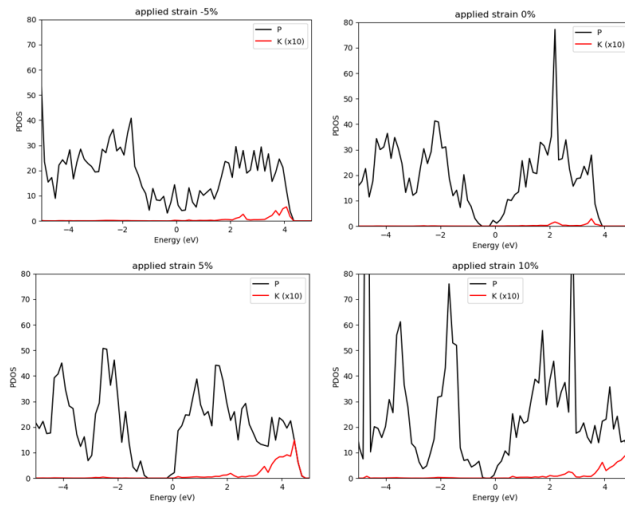


Figure 40: The projected density of states shown for phosphor atoms, and the potassium atom separately, for the models of phosphorene with an adsorped potassium atom on the H site for 0%, -5%, 5%, and 10% strain, respectively. For the contribution of the potassium states, the values are multiplied by 10 to improve visualization.

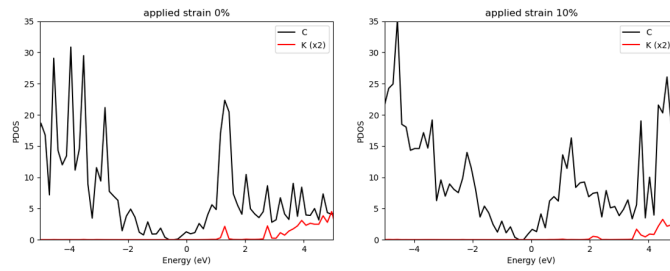


Figure 41: The projected density of states shown for carbon atoms, and the potassium atom separately, for the models of graphene with an adsorped potassium atom on the H site for 0% and 10% strain, respectively. For the contribution of the potassium states, the values are multiplied by 2 to improve visualization.

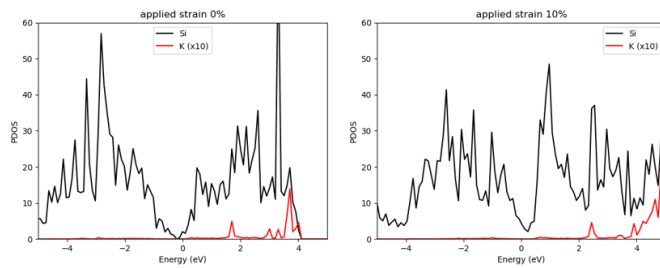


Figure 42: The projected density of states shown for silicon atoms, and the potassium atom separately, for the models of silicene with an adsorped potassium atom on the H site for 0% and 10% strain, respectively. For the contribution of the potassium states, the values are multiplied by 10 to improve visualization.

Appendix G: Bader charges

Vacancy defects

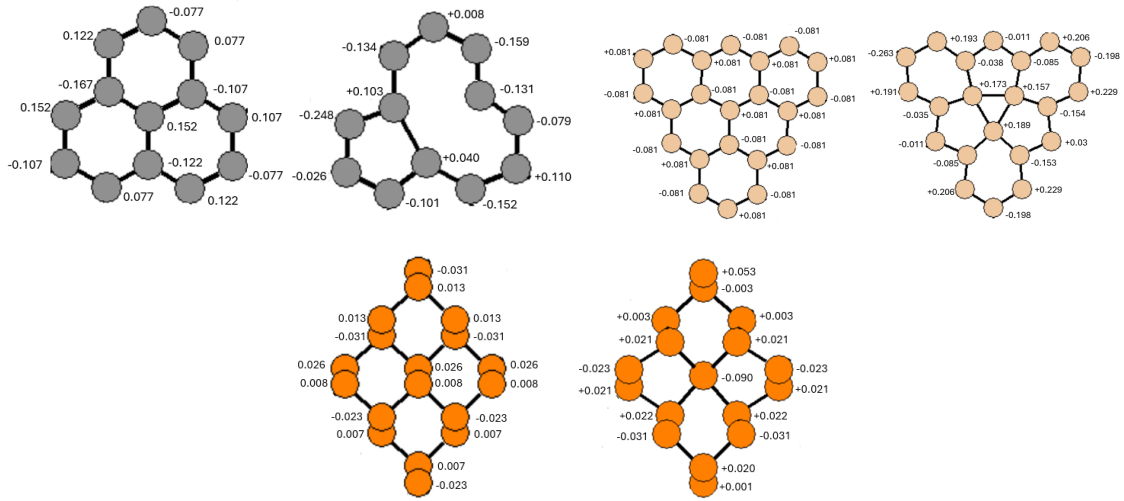


Figure 43: The Bader charges of the pristine models are shown on the left, with the change in Bader charge upon the introduction of a vacancy defect on the right, for graphene, silicene, and phosphorene, respectively.

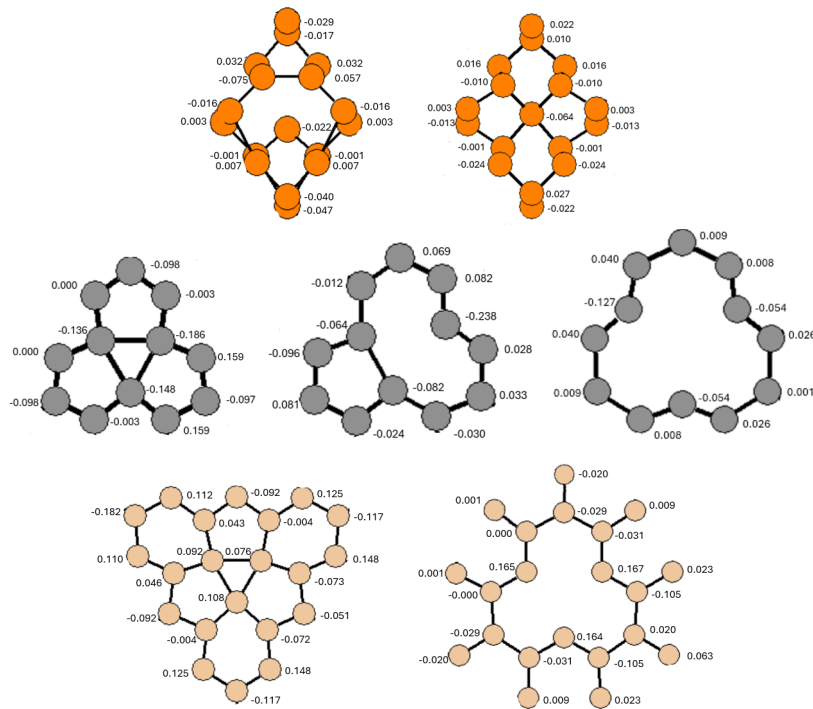


Figure 44: The Bader charges of the atoms surrounding the vacancies for various strained models for each of the materials. For graphene, the -5%, the 0%, and the 10% vacancies are shown. For silicene, the 0% and 10% and for phosphorene the -5% and 0%.

Potassium adsorption

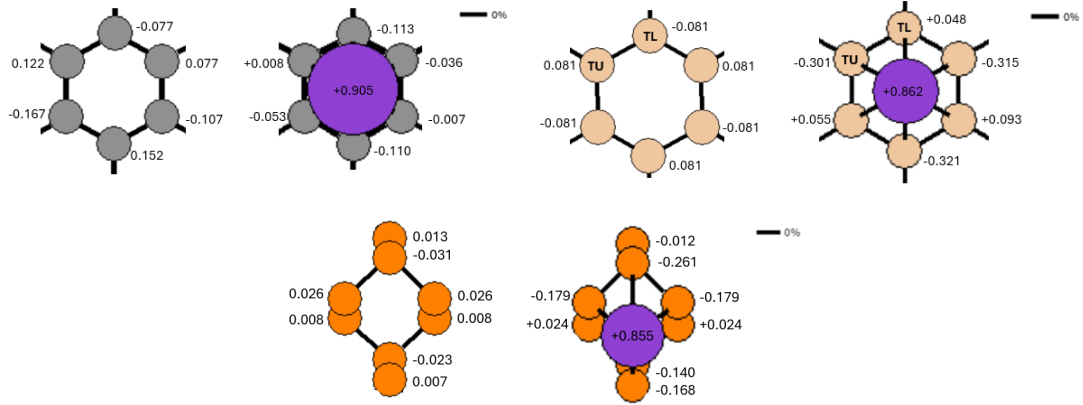


Figure 45: The Bader charges of the pristine models are shown on the left, with the change in Bader charge upon potassium adsorption on the right, for graphene, silicene, and phosphorene, respectively.

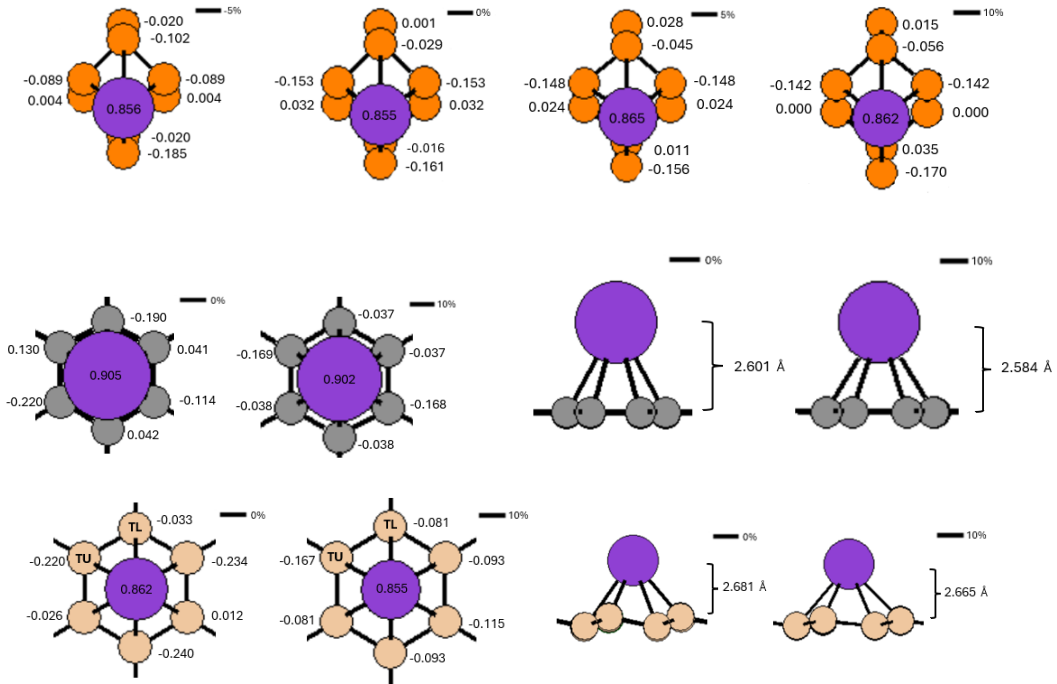


Figure 46: The Bader charges are shown for the potassium atom and atoms surrounding the adsorption site for each of the materials. For graphene and silicene, the Bader charges are shown for the 0% and 10% strained models. Additionally, the distance of the potassium atom to the surface is shown. For phosphorene, the Bader charges are shown for the adsorption sites located in the -5%, 0%, 5% and 10% strained models.